KU LEUVEN

FACULTY OF SCIENCE

Elastic scattering and cluster-transfer reactions of ^{98}Rb on ^{7}Li at REX-ISOLDE

CERN-THESIS-2013-436
/ /2013

Jake BOUMA

Supervisor: Prof. R. Raabe
Co-supervisor: Freddy Flavigny

Thesis presented in
fulfillment of the requirements
for the degree of Master of Science
in Nuclear Physics

Academic year 2012-2013
(reviewed version)

Acknowledgements

Though a proud South African, it was always a goal of mine to study abroad. This was made possible by the Erasmus Mundus Action 2 scholarship programme, to whom I am truly grateful. My two year stay in Belgium has been a fantastic experience both academically and otherwise.

The Instituut voor Kern- en Stralingsfysica (IKS) has been incredibly accomodating. Particular thanks are in order for their support for me to visit CERN. Visiting the facility and taking part in an experiment at ISOLDE is something that I did not even imagine to be possible.

My master thesis has been a great learning experience, especially due to wonderful people that helped me along the way and the particularly friendly research group. The discussions that I have had with R. Raabe, F. Flavigny, S. Bottoni and R. Orlandi perhaps gave me more insight into nuclear physics than all the courses I have taken thusfar. This made the work for my master thesis especially rewarding. I leave Belgium with a great fondness for Leuven and KULeuven, proud of the masters programme I have graduated from.

Summary

Exotic nuclei are nuclei with unusual proton to neutron ratios that exist far away from stability. Due to their instability, these nuclei are only available for nuclear reactions as radioactive ion beams. Experiments must therefore be performed in inverse kinematics at advanced radioactive isotope separation and acceleration facilities. REX-ISOLDE at CERN is one such facility, capable of producing post-accelerated radioactive ion beams with energies up to 2.85 MeV/u.

Cluster-transfer reactions in inverse kinematics with a ^{7}Li target are proposed as a tool for the study of exotic nuclei at REX-ISOLDE. In these reactions, either the α or triton clusters that make up the weakly bound ^{7}Li nucleus can be transfered to the beam nucleus. The remaining cluster that is not transferred can be detected, and identifies the particular transfer channel. Through this mechanism it is possible to populate states of very high spin, which is useful for γ-spectroscopy in poorly known exotic regions.

Specific regions of interest for these reactions are around doubly magic nuclei. Here adjacent nuclei are well described by valence nucleons interacting around the inert core. In particular the doubly magic ^{132}Sn nucleus is also very neutron rich and serves as an ideal base from which to study changes in nuclear structure away from stability.

Currently however, these very massive nuclei of interest are inaccessible to cluster-transfer reactions with ^{7}Li at REX-ISOLDE due to the high Coulomb barriers. In anticipation of the upgraded post-acceleration of HIE-ISOLDE that is currently being implemented, a preliminary experiment was performed with REX-ISOLDE to study the cluster-transfer reactions of the ^{98}Rb + ^{7}Li system.

This experiment provides much needed experience and insight into the particularities of cluster-transfer with ^{7}Li. Analysis performed for this masters thesis focused on the analysis of the detected particles. The elastic scattering channel was carefully treated to determine a scaling factor with which the absolute differential cross-sections for the detection of α-particles and tritons could be scaled. The cross-sections for α- and triton transfer were found to be larger than expected, boding well for future studies.

The measured cross-sections were compared to theoretical calculations. A preliminary Continuum Discretized Coupled Channels (CDCC) calculation, which took into account the observation that the cluster transfer was occuring to high excitation unbound states, was able to reproduce well the data. Concerning the γ-rays, we indeed observed states of the residual nuclei at very high angular momenta.

This thesis concludes with a discussion of the potential of cluster-transfer reactions going forward, in light of what we observe in this experiment. Important practical insights regarding the detection of particles are given and the possibilities for producing more exotic nuclei are given.

Nederlandse Samenvatting

Exotische kernen zijn kernen met een ongebruikelijke verhouding tussen het aantal protonen en neutronen. Deze kernen zijn vaak heel instabiel, waardoor ze enkel met kernreacties bestudeerd kunnen worden in radioactieve bundels. Experimenten moeten daardoor uitgevoerd worden in inverse kinematica, en dat in geavanceerde faciliteiten die radioactieve isotopen kunnen separeren en versnellen. REX-ISOLDE in CERN is een voorbeeld van zo'n faciliteit en is in staat om versnelde radiactieve bundels te produceren met energieën tot en met 2.85 MeV per nucleon.

Cluster-transfer reacties in inverse kinematica met een ^{7}Li trefschijf zijn voorgesteld als een manier om exotische kernen te bestuderen in REX-ISOLDE. In deze reacties kan ofwel het alfa-deeltje of het tritium-deeltje die een deel uitmaken van de ^{7}Li kern overgebracht worden naar de kern in de bundel. Het overblijvende deeltje dat niet getransfereerd is kan gedetecteerd worden en dient als een vingerafdruk voor het reactiekanaal dat opgetreden is. Via dit mechanisme is het mogelijk om toestanden met een hele hoge spin te bevolken, wat nuttig is voor γ-spectroscopie in weinig gekende regios van de kernkaart.

Interessante regios voor deze reacties zijn de kernen in de buurt van de dubbelmagische kernen. De nabijliggende kernen kunnen goed beschreven worden via valentienucleonen die rond de inerte kern interageren. De dubbelmagische kern ^{132}Sn is een is een neutronrijke kern die ideaal geschikt is om de veranderingen in kernstructuur ver weg van stabiliteit te bestuderen.

Helaas zijn deze interessante, massive kernen niet bereikbaar om via cluster-transfer reacties met ^{7}Li te bestuderen in REX-ISOLDE omwille van de hoge Coulomb-bariére. In afwachting van de upgrade van de post-acceleratie van HIE-ISOLDE die op het moment van schrijven aan de gang is, werd een experiment op REX-ISOLDE uitgevoerd om de cluster-transfer reacties van het ^{98}Rb + ^{7}Li systeem te bestuderen.

Dit experiment biedt broodnodige ervaring en inzichten in de eigenschappen van cluster-transfer reacties met ^{7}Li. De analyse die werd uitgevoerd in deze thesis plaatst zijn focus op de analyse van de gedetecteerde deeltjes. Het elastische verstrooiingskanaal werd zorgvuldig behandeld om een schaalfactor te bepalen waarmee de absolute differentiële botsingsdoorsnedes voor de detectie van α-deeltjes in tritium herschaald kunnen worden. Deze botsingsdoorsnedes bleken groter dan verwacht, wat goed nieuws is voor verdere studies.

De gemeten botsingsdoorsnedes werden vergeleken met theoretische berekeningen. Een voorlopige berekening met Continuum Discretized Coupled Channels (CDCC) die rekening hield met de observatie van clustertransfer naar hooggelegen ongebonden toestanden kon de data goed reproduceren. De γ-straling van de bijhorende resterende kernen met hoge angulaire momenten werd inderdaad geobserveerd.

Deze thesis concludeert met een discussie van het potentieel van cluster-transfer reacties voor de toekomst, in acht nemende wat dit experiment ons leerde. Belangrijke praktische inzichten betreffende de detectie van deeltjes worden gegeven en mogelijkheden voor het produceren van meer exotische kernen worden besproken.

Contents

Chapter 1

Introduction

1.1 Nuclear structure and exotic nuclei

The chart of nuclides (figure 1.1) is a good starting point for any discussion of nuclear structure. Nuclei consist of a certain number nucleons – protons and neutrons – and are arranged in this chart accordingly. An arrangement of protons alone would be unbound, due to the coulomb repulsion between the positively charged particles. The attractive nuclear force acts between nucleons and can counterbalance the effect of the coulomb force to break apart the nucleus. A bound or stable nucleus has the correct number of protons and neutrons such that the repulsive coulomb force is overcome. These are the nuclei that appear as the backbone of the chart of nuclei, forming what is known as the valley of stability.

One of the first and most useful models of nuclear structure is the Shell model [1]. This idea began with the striking observation of *magic* nuclei – especially stable nuclei with proton and/or neutron numbers equal to 2, 8, 20, 28, 50, 82 and 126 – which indicated a shell structure analogous to that of atomic electron configurations. Such behaviour would not be reproduced by a liquid drop model, for example. The challenge was then to find an adequate potential for the system of nucleons which would at the very least reproduce the observed magic numbers. This was finally done in 1950 when the spin orbit interaction, whose contribution had been somewhat underestimated, was included [2]. Since then, the shell model has been the basis for explaining nuclear structure.

Many refinements have been added to the shell model over the years, but the premise remains much the same. Several new theories have also emerged from ideas of the shell model, warranting the award of the Nobel prize in 1966 to the pioneers of the theory. However, this model is based on some fairly precarious assumptions.

The first important assumption of the Shell model is that of spherical symmetry. Near the magic numbers that the model reproduces, this assumption is acceptable. However, away from shell closures nuclei can become deformed, and refinements or other models are required. For example the deformed shell model or Nilsson model [3] extends the ideas of orbitals and shell structures to deformed nuclei.

The second assumption is that of independent particles. Protons and neutrons occupy energy levels in an effective potential and do not see each other. Modern shell model calculations account for interactions between nucleons in different orbitals, but the model space can be so large for heavy nuclei that an assumption of an inert core at some level must be made to have a workable model space.

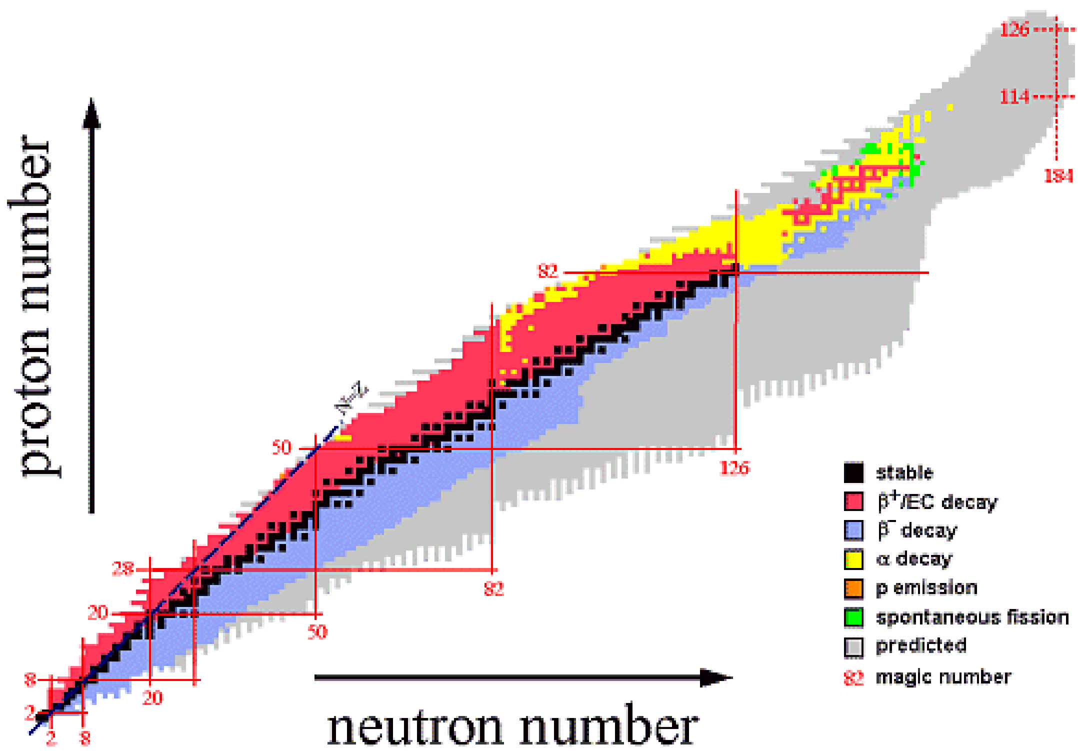

Figure 1.1: Chart of nuclides. Stable nuclides are shown in black, at the bottom of the so called "Valley of Stability" in the nuclear landscape. Unstable nuclei that decay predominantly via β^+ decay or eletron capture are shown in red, and by β^- decay in blue. Unknown nuclei (not yet studied experimentally) are shown in grey up to the predicted limits of nuclear existence – the proton and neutron drip lines. Fissioning nuclei are shown in green and only appear at heavier masses.

The more nuclei we study, the more tests we have for models such as the Shell model. Stable nuclei are for obvious reasons more easily studied. Therefore the refinement of the shell model potentials for example, has been biased towards the valley of stability. In predicting the structure of these nuclei, our theories are well matured. However, for *exotic nuclei* away from stability, this is not the case.

Exotic nuclei are nuclei with an unusual proton to neutron ratio. They can be either rich or poor in neutrons compared to their stable isotopes at the line of stability. Such nuclei will typically undergo beta decay back towards more tightly bound nuclei at the bottom of the valley of stability. This makes them short-lived and therefore difficult to produce and study.

Exotic nuclei exist within the limits of the drip lines. Far enough from stability on the neutron rich side nuclei become unstable against neutron emission and we reach the neutron drip line. Beyond this limit nuclei are unbound. Similarly on the neutron deficient (proton rich) side we encounter the proton drip line as nuclei become unstable to proton emission. The proton drip line lies much closer to stability because the effect of the Coulomb force to break apart the nucleus increases as the proton to neutron ratio increases. Finally, towards very heavy nuclei fission begins to limit stability. Spontaneously fissioning nuclei are shown in figure 1.1 in green. It is predicted that between the drip lines there exist some 7000 nuclei, most of which are are yet to be studied.

As experimental techniques have matured, we have become able to produce and study increasingly exotic nuclei. Not surprisingly, predictions of the shell structure of these nuclei with models that were obtained from data at stability have had limited success. Several unexpected phenomena have emerged, and will surely help to better the understanding of nuclear structure.

The evolution of shell structure away from stability is of most interest. Nuclei with unexpected shell model state ordering are commonly observed, and ground state inversion, which was previously confined to an "Island of Inversion" has been noticed in a wide range of nuclei [4]. Such observations must be understood by refining or redefining models, and will hopefully reveal new aspects of the nuclear force.

The study of deformation and collective behaviours of non-spherical nuclei is of equal importance. The most striking example thereof is in the neutron deficient Pb isotopes, where Shape Coexistence [5] – the competition of different shapes at comparable energies – is clearly observed. This phenomena has been observed across the nuclear landscape, but due to difficulties in producing exotic nuclei, is not too well studied in the very neutron poor Pb isotopes where it appears to be strongest.

Studies of the interaction between nucleons in exotic nuclei will also aid in its understanding. Although the nuclear force is known to be a manifestation of quark interactions described in the standard model, the energy scales of nuclear physics are well below those of particle physics, and so a nucleon-nucleon potential is used. To study the nuclear force in nuclei, we can look to near spherical nuclei at magic numbers. Adjacent nuclei with a few nucleons or holes above an inert core provide a simplified model space where we can look at the interactions of valence nucleons with the core and with eachother in the environment of the core. The region around ^{132}Sn for example is of particular interest, because this nucleus is exotic and doubly magic.

A final reason for studying exotic nuclei on the neutron rich side lies in nuclear astrophysics. The nucleosynthesis of the heaviest elements is believed to occur via the rapid capture of neutrons under extreme stellar conditions of neutron density and temperature (r-process). Nuclei increase rapidly in mass along a path through the very neutron rich nuclei. Understanding the rapid neutron-capture process (r-process) relies heavily on the accuracy of data in the neutron rich region. Current uncertainties for unstudied nuclei are high, for example uncertainty in masses are of the order MeV. This uncertainty blows up upon extrapolation to astrophysical conditions which are generally not experimentally reproducible on Earth. To be able to simulate the r-process more comprehensive data in the neutron rich region is needed.

To summarize - the systematic study of exotic nuclei is important for three main reasons:

1. To test, refine and develop models for nuclear structure by acquiring new data. This data is also useful for astrophysical calculations and predictions.
2. Exploration; to discover new behaviours and understand their consequences for theoretical pictures.
3. To determine the limits of nuclear existence by studying nuclei at the drip lines.

1.2 Nuclear Reactions

In this work we are concerned with nuclear reactions as a tool for studying these exotic nuclei. In a two-body nuclear reaction, a *projectile* nucleus is accelerated in a beam and collided with a *target* nucleus. Different processes can occur, producing particles and/or γ-rays, depending on the beam energy and interacting nuclei. In experiments we detect the particles and/or γ-rays from the reaction, and reconstruct the reaction to learn about the structure of involved particles or the reaction mechanism itself.

Nuclear reactions studied with beams on targets are typically two-body processes. The most convenient reference frame is therefore the center of mass (CM). In the CM frame the momentum of both particles are the same, and which particle was accelerated is irrelevant. This allows us some choice as to which particle we choose to accelerate. In *direct kinematics* the light particle in the reaction is accelerated onto the stationary heavy target. In *inverse kinematics* the heavy particle is accelerated. The description of the scattering in the center of mass frame is the same in both cases, save the difference in the transformations to get there. Inverse kinematics are necessary for the study of reactions with exotic nuclei, which are too unstable to play the role of the target, and are only available as Radioactive Ion Beams (RIB). Such beams of exotic nuclei are only recently available thanks to the technical development of the ISOL (Isotope Separation Online) technique for isotope production, of which ISOLDE (ISOL Device) is a foremost example [6]. The In-flight technique is another popular means radioactive isotope production [7]. High energy beams are created by efficient post-acceleration of separated ions. At ISOLDE this is provided by the REX (Radioactive beam EXperiment) post-accelerator complex.

Depending on the nuclei and the energy, several nuclear reactions are possible in beam on target experiments. In *fusion-evaporation* reactions, the projectile nucleus fuses with the target nucleus, forming a compound nucleus at high excitation energy. This compound nucleus can de-excite by ejecting particles (typically neutrons) to lose energy in a manner resembling evaporation from a hot liquid. In such a reaction, the formation of the compound nucleus and its decay are two independent steps where the compound system has no memory of the entrance channel. In *direct* reactions on the other hand, the exit channel is strongly coupled to the entrance channel. Such reactions include elastic and inelastic scattering, and are characterized by fast, peripheral collisions, without the formation of an intermediate quasibound state. In reality a nuclear reaction can demonstrate both direct and compound behaviour. One should not lose sight of the fact that experimentally, what we can observe are the incident particles before the reaction and the outgoing particles after the reaction. By looking at the angular distributions of the outgoing particles we can sometimes clearly identify a reaction mechanism or separate what we observe into direct and compound contributions – but not always. There is indeed a grey area between the direct and fusion reaction mechanisms.

In *massive transfer reactions* we observe a redistribution of mass in the nuclear reaction. Typically, a light nucleus interacts with a heavy nucleus, with the transfer of mass leaving the heavy *residual* nucleus in an excited state. Different types of massive transfer reactions are shown in figure 1.2. The simplest case is the redistribution of a single nucleon. The removal of a nucleon is studied in *knockout* reactions – where a nucleon is removed but not captured and three particles scatter in the exit channel – or *pickup* reactions – where the removed nucleon is captured by the scattered projectile nucleus.

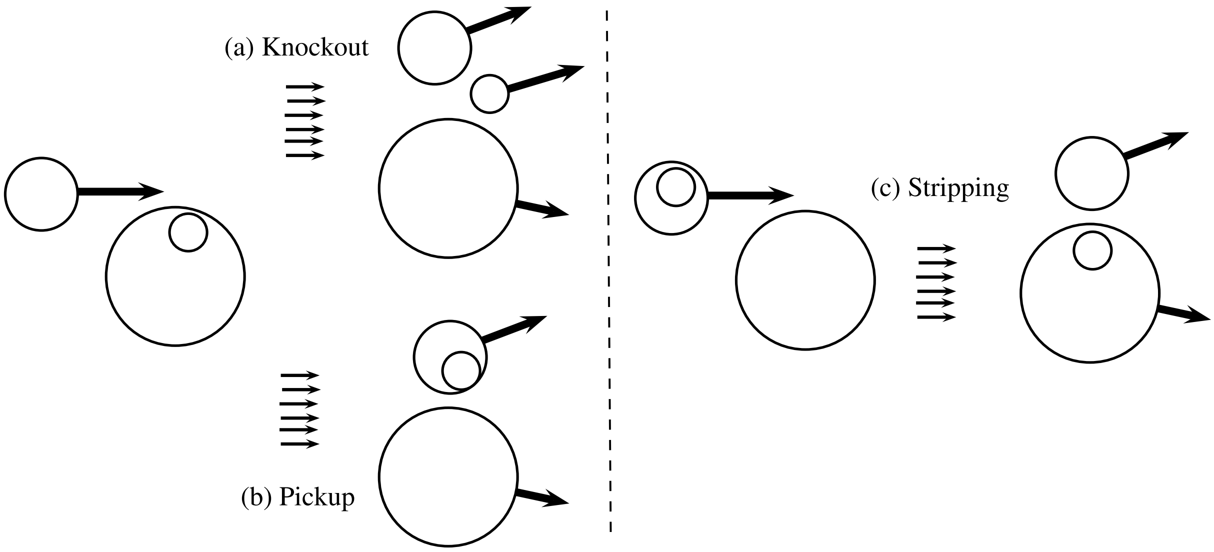

Figure 1.2: Different types of transfer reactions.

The hole left by the removed nucleon leaves the residual nucleus in a specific excited state. In *stripping reactions*, a nucleon is transferred to the heavy nucleus from the projectile, for example single neutron transfer with a deuteron projectile, (d,p). In such reactions, the nucleon is transferred to a single particle state in the residual nucleus.

The nature of single-nucleon transfer reactions is direct, allowing us to probe directly the single particle states in the residual nucleus. The binding of a single nucleon in a nucleus can be considered as a result of the average potential due to the other nucleons. Nucleons occupy single-particle eigenstates in this average potential, that are independent of one another in a first approximation. We can understand these transfer reactions as the direct transfer to/from the single particle states in the residual nucleus. This simple picture overlooks higher order effects and correlations between particles. Transfer reactions allow us to study how well the state of the nucleon can be described by single particle motion in the nucleus.

Not surprisingly, the exchange of more than just a single nucleon in a reaction is possible. Several nucleons, or a bound or quasibound cluster of nucleons can be redistributed from one nucleus to another. Along with the mass comes a large amount of excitation energy, which is typically released by the evaporation of neutrons. Early studies for example focused on the transfer of α-clusters from ^{12}C to a heavy ^{160}Gd target using particle-γ coincidence measurements [8]. Recent focus is on the transfer of α-particles and tritons from the weakly bound ^{7}Li nucleus [9, 10].

Such reactions go by several names – multinucleon massive transfer, incomplete fusion, cluster-transfer and deep-inelastic scattering – each of which paint a particular picture of the reaction mechanism that leads to *the same* net redistribution of mass. The seeming ambiguity is a result of the combination of direct and fusion-like charateristics of the reaction. In this thesis, the name *massive transfer* will be used to refer to the above-mentioned process, irrespective of the theoretical description.

The description of *cluster-transfer* is a natural extension of single-nucleon transfer – a cluster of particles are inserted into a cluster-particle state in the residual nucleus. This is a direct reaction description. The *incomplete fusion* (IF) descriptions on the other hand, treat the exchange of mass as a fusion process. *Breakup-fusion* for example first treats the breakup into clusters, then the fusion of a cluster with the heavy nucleus. In this thesis will assume the cluster-transfer mechanism to interpret the observations, unless explicitly stated otherwise.

Experimentally, both single nucleon transfer and massive transfer reactions have the advantage that detection and identification of one of the particles in the exit channel can be used to flag the transfer process. For example, the detection of protons in an experiment with deuterons on a heavy nucleus can be used to separate the (d,p) neutron transfer channel. This information greatly complements spectroscopic information through particle-γ coincidence. Secondly, the energy of the light outgoing particles associated with the transfer channel can be used to reconstruct the kinematics of the scattering, giving the excitation energy of the residual nucleus. In single nucleon transfer, this can be directly related in a direct reaction picture to the energy of the single particle state to (from) which the transfer (pickup) occurred. For the transfer of a cluster the analogous direct-reaction interpretation would be the energy at which the cluster is transfered to the residual nucleus, which could be interpreted in terms of a Cluster model.

Massive transfer reactions, at the expense of significant complexity in the description of the reaction mechanism, are able to populate much higher angular momentum in the residual nucleus than conventional single-nucleon transfer reactions. This is simply due to the larger mass transferred to the residual nucleus, which also offers us new ways to produce certain nuclei.

Clearly a large variety of methods are available to probe the nucleus. Depending on the physics case a single type of reaction is normally the focus of a single experiment.

1.3 Experimental Proposal

Cluster-transfer reactions have been identified as a useful reaction for acquiring spectroscopic information in exotic and stable nuclei. Their ability to (1) populate states of high angular momentum, (2) transfer greater mass than conventional transfer reactions to possibly form even more exotic nuclei and (3) provide a trigger of reaction channels with particle detection make them very attractive.

Cases of special interest for the application of these reactions are the doubly magic ^{132}Sn and ^{208}Pb nuclei [11]. Such nuclei are well described as closed shells, making them particularly useful for the study of nearby systems with particles/holes in excess of the closed shell. How well the nearby nuclei can be described as valence nucleons interacting with an inert core is an important test of nuclear structure. Both the single particle energies of the nucleons near the closed shells and the two-body matrix elements of the effective nuclear interactions can be extracted [11] from studies of the nearby nuclei.

^{132}Sn in particular, is a very neutron rich exotic nucleus. This makes it an ideal stepping stone from which to explore the structure of nearby exotic nuclei. ^{132}Sn, not surprisingly with its large proton-neutron asymmetry, is unstable, with a lifetime of 39.7s. Nuclear reactions must therefore be performed in inverse kinematics, using a Radioactive Ion Beam. REX-ISOLDE[1] [12] is a post-accelerated radioactive ion beam facility at CERN, producing beams at an energy of up to 2.85 MeV/u. Cluster-transfer reactions with ^{7}Li are proposed, to populate nuclei in regions of interest such as the case of ^{132}Sn.

[1]**R**adioactive beam **ex**periments at ISOLDE (**I**sotope **S**eparation **On**line **D**evice)

However, the current beam energy available at REX-ISOLDE is insufficient for such a reaction. The above-mentioned areas of study are therefore forward thinking, in anticipation of the HIE-ISOLDE (High Ion Energy ISOLDE) upgrade that is currently underway. The upgraded facility will include further post acceleration of the RIB in two stages, reaching energies of 5.5 MeV/u in 2014 and 10 MeV/u by its completion. In the meantime, because of lack of experience with cluster-transfer reactions with ^{7}Li in inverse kinematics, a somewhat preparatory study was performed at ISOLDE. A beam of ^{98}Rb at 2.85 MeV/u was used to study cluster-transfer reactions with a ^{7}Li target.

By studying this system we hope to gain insights into what is possible with cluster-transfer reactions at HIE-ISOLDE. To proceed confidently towards very exotic heavy nuclei like ^{132}Sn, we must understand both the reaction mechanism and the expermental aspects of cluster-transfer better. The ^{7}Li target nucleus can be considered as a weakly bound α-t system, and can transfer either one of these clusters (among other channels). Estimates for the cross-sections for these processes are very unreliable, because of the complexity of the theory of cluster-transfer reactions. Measuring the cross-sections for these channels and comparing them to new and existing theoretical models will allow us to make better estimates of the cross-sections in future experiments. These cross-sections are very low, and so such extrapolations are key in assessing the feasibility of future experiments.

As important as the theoretical considerations to the feasibility of future studies, are the experimental limitations. Understanding what is required from the beam, detector setups and data acquisition for the particular case of a ^{7}Li target allows us to estimate statistics and resolution attainable in future experiments. For a simple example, particularities involving the detection of tritons, α-particles and lithium isotopes, which are heavier than the usual transfer ejectiles treated at REX-ISOLDE.

This thesis aims to provide early insights into what we could expect from cluster-transfer reactions at HIE-ISOLDE, by focusing on the light ejectile particles. The analysis of detected particles was a large part of the work for this thesis. The elastic scattering channel is carefully treated to extract a scaling for the differential cross-sections of the transfer reaction channels. The resulting cross-sections are then compared to theoretical calculations. Practical suggestions are put forward for future experiments, and a discussion of the feasibilty of cluster-transfer reactions in studying exotic nuclei is made.

Chapter 2

Theoretical descriptions

A theoretical description of massive transfer is complicated by the combination of direct and fusion-like character of the process. For this reason, several interpretations exist, some of which are more successful under certain conditions. Figure 2.1 shows schematically the system that we are trying to describe. A weakly bound nucleus A=a+x interacts with another (typically much heavier) nucleus b. After the interaction we observe what remains of the light particle, a, after it has given some of its mass to the heavy nucleus b, and the heavy particle, which in some reaction mechanism accepted the mass and energy from the light nucleus and evapourated neutrons to ease the excitation energy. The grey area in figure 2.1 emphasizes the fact that we must propose a reaction mechanism to explain what we observe.

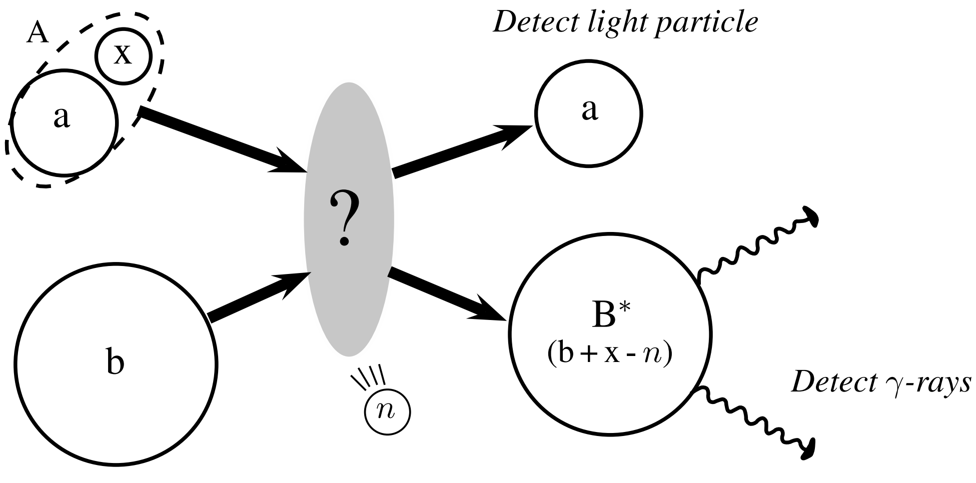

Figure 2.1: Schematic of massive transfer reaction mechanism.

In this chapter two models of the reaction mechanism are presented in anticipation of their comparison with experimental results: a semi-classical Sum-rule model of incomplete fusion and cluster-transfer. Elastic scattering is an important part of this thesis as it allows us to extract a scaling factor for the differential cross-sections of the other reaction channels. How optical model calculations of elastic scattering can be performed is therefore described in some detail.

2.1 Sum-rule model of incomplete fusion

Early descriptions of the reaction mechanism were those of incomplete fusion in the late 70s. A combination of statistical and direct aspects were observed in the reactions and were discussed by Bondorf et al. [13] in 1971. This led in part to the formulation of a Sum-rule model by Wilczyński et al. [14]. This semi-classical model provides an intuitive picture of the angular momentum considerations of massive transfer, though it is quantitatively of little use.

2.1.1 Generalized Concept of Critical Angular Momentum

Key in the incomplete fusion description of [14] is the treatment of angular momentum in the entrance channel by extending the idea of critical angular momentum for complete fusion [15]. For the complete fusion of a projectile nucleus with the target nucleus there is a *critical angular momentum* of the pair's relative motion, l_{crit}, above which the process does not occur. The critical angular momentum for complete fusion can be calculated by so called "balance of forces". This calculation is done in detail in the framework of a liquid drop model in ref. [15]. The premise of the calculation is to balance the nuclear, coulomb and centrifugal forces at the point where the nuclear force is strongest. At $l > l_{\mathrm{crit}}$ the attractive nuclear force is overwhelmed by the repulsive coulomb and centrifugal forces so complete fusion cannot occur. The result of the calculation is [8]:

$$(l_{\mathrm{crit}} + \frac{1}{2})^2 = \frac{\mu(C_1 + C_2)^3}{\hbar^2}\left[4\pi\gamma\frac{C_1C_2}{C_1+C_2} - \frac{Z_1Z_2e^2}{(C_1+C_2)^2}\right] \tag{2.1}$$

where C_1,C_2 and Z_1,Z_2 are the half density radii and proton numbers of the projectile and target nuclei respectively. γ is the surface tension coefficient from the liquid drop treatment of the nuclear force and μ is the reduced mass of the binary system.

The cross-section for complete fusion can then be calculated for partial waves with angular momentum l up to the critical angular momentum:

$$\sigma_{\mathrm{CF}} = \frac{\pi\hbar^2}{2\mu E}\sum_{l=0}^{l_{\mathrm{crit}}}(2l+1)T_l = \frac{\pi\hbar^2}{2\mu E}(l_{\mathrm{crit}}+1)^2 \tag{2.2}$$

where T_l is the transmission coefficient for orbital momentum l [1]. This simple model has been successful in reproducing the important dependencies of the cross-section on the charges and mass numbers of the binary systems [8].

The next step is to assume that complete and incomplete fusion reactions can be understood as different realizations of the same mechanism [8]. This is supported by early observations of Bondorf et. al. [13] and allows for the concept of critical angular momentum to be extended to incomplete fusion.

It is convenient to label the incomplete fusion reaction channels, namely transfer of one nucleon, two nucleons, and so on up to complete fusion, by i. There is then a critical angular momentum for each channel i above which it will not occur. The critical angular momentum for fusing a fragment of the projectile in a reaction channel i can be calculated

[1] T_l must go to zero for $l > l_{\mathrm{crit}}$, so cutting the sum at l_{crit} is not necessary, but is included for emphasis.

with equation 2.1 after substituting the projectile with the fragment. Assuming that any virtual fragment of the projectile nucleus carries angular momentum proportional to its mass we can obtain a *limiting angular momentum* $l_{\rm lim}(i)$ in the entrance channel – a maximum angular momentum for each incomplete fusion reaction i. Namely,

$$l_{\rm lim}(i) = \frac{A_{\rm proj}}{A_{\rm cap}(i)} l_{\rm crit}(i) \tag{2.3}$$

where $A_{\rm proj}$ and $A_{\rm cap}$ are the atomic masses of the complete projectile and fused fragment respectively. For example a triton (^{3}H) fragment in a ^{7}Li projectile would carry a fraction of $\frac{3}{7}$ of the relative angular momentum of the projectile-target system. This fraction must be less than the critical angular momentum for the triton-target nucleus system for triton fusion to occur. The remaining angular momentum is carried away by the unfused α-particle. Figure 2.2 shows the limiting angular momenta for incomplete fusion channels of a ^{7}Li nucleus.

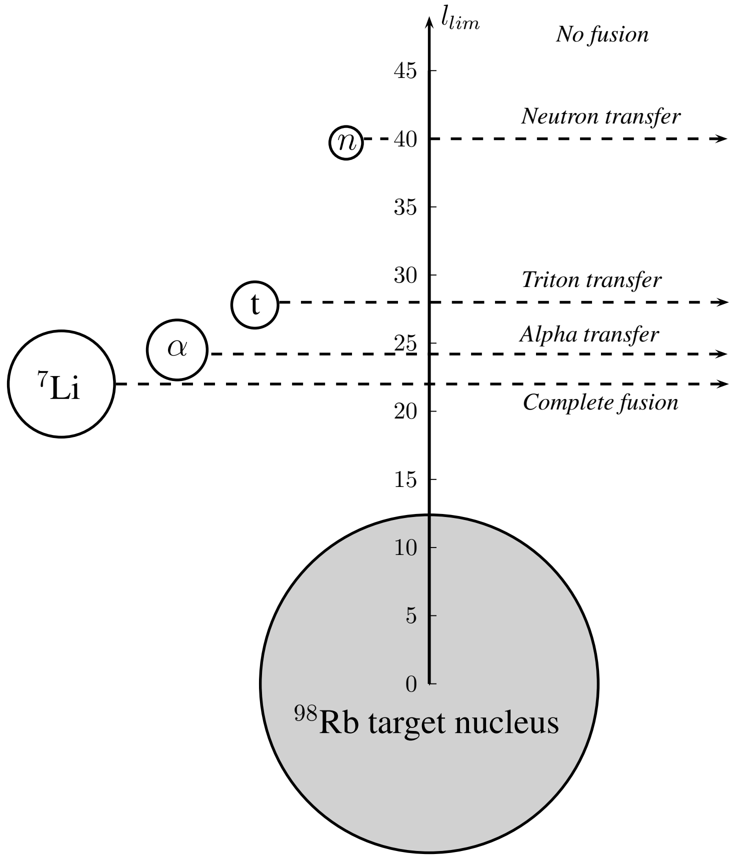

Figure 2.2: Generalized limiting angular momenta for selected incomplete fusion channels of ^{7}Li and ^{98}Rb. The light particles should be viewed as fragments of ^{7}Li. If the total angular momentum of ^{7}Li exceeds the limiting angular momentum indicated by a fragment, incomplete fusion cannot occur.

2.1.2 Sum-Rule Model

Like the concept of generalized angular momentum presented above, the Sum-rule model of Wilczyński et al. [14] handles all reaction channels i, complete and incomplete, in the same manner. Under this assumption we can generalize equation 2.2 to incomplete fusion channels. The different channels' limiting angular momenta and their relative strengths need to be included. Assuming the total cross-section to be divided amongst all the reaction channels, the cross-section for each channel can be expressed as a Sum-rule [14]

$$\sigma(i) = \frac{\pi\hbar^2}{2\mu E}\sum_{l=0}^{l_{\max}}(2l+1)\mathcal{P}_l(i) \tag{2.4}$$

where $\mathcal{P}_l(i)$ represents the normalized contribution of channel i such that $\sum_i \mathcal{P}_l(i) = 1$ and $l_{\max}$ is the maximum angular momentum for which any incomplete fusion can take place. Considering figure 2.2 for the case of a ^{7}Li, $l_{\max}$ would correspond to the $l_{\lim}$ of neutron transfer.

It had been experimentally observed that the probability for a reaction channel i is proportional to exponential of the ground state Q-value, Q_{gg} [13]. Characteristics of both direct and statistical mechanisms were also observed. In light of this Bondorf et al. [13] proposed a partial statistical equilibrium of the system postulating for the probability of a fusion channel i

$$p(i) \propto \exp(\frac{Q_{gg}(i) - Q_c(i)}{T}) \tag{2.5}$$

where T a free parameter and Q_c is the difference in the Coulomb interaction energy that is included to account for the transfer of charge from the projectile to the target. It can be expressed as

$$Q_c \approx (Z_1^f Z_2^f - Z_1^i Z_2^i)e^2/R_C \tag{2.6}$$

where $Z_1^f Z_2^f$ and Z_1^i, Z_2^i are the proton numbers of the final and initial dinuclear systems respectively and R_C is the effective Coulomb interaction radius. Though R_C is considered a free parameter it is expected to be approximately equal to the sum of the radii of the two interacting nuclei $R_C \simeq 1.5(A_1^{1/3} + A_2^{1/3})$ [16].

The limiting angular momentum for process i is calculated with equations 2.1 and 2.3. Above its $l_{\lim}$, an incomplete fusion channel should close. This behaviour can be included in a transmission coefficient. Assuming a smooth cutoff with sharpness Δ (the same for all channels), the transmission coefficients $T_l(i)$ are given by

$$T_l(i) = \left[1 + \exp\left(\frac{l - l_{\lim}(i)}{\Delta}\right)\right]^{-1} \tag{2.7}$$

Combining the probability and the transmission coefficients with an appropriate normalization yields the Sum-rule for the cross-sections of each channel

$$\sigma(i) = \frac{\pi^2\hbar^2}{2\mu E}\sum_{l=0}^{l_{\max}}(2l+1)\frac{T_l(i)p(i)}{\sum_j T_l(j)p(j)} \tag{2.8}$$

Wilczynski et al. [16] performed calculations for the $^{14}\mathrm{N} +^{159}\mathrm{Tb}$ system at an energy of 14 MeV/u ^{14}N. In this experiment the calculations *fitted* the experimental results well. The three free parameters of the model, were found to be

$$\begin{aligned} T &= 3.5\ \mathrm{MeV} \\ R_C &= 1.5\,\mathrm{fm} \\ \Delta &= 2 \end{aligned} \tag{2.9}$$

The model has been applied with similar parameter sets to the fairly similar $^{14}N+^{154}Sm$ [17] and $^{12}C+^{160}Gd$ [18] systems, with agreeable results. The main advantage of this model is its simplicity. Detailed agreement with experiments cannot be expected. Recently, a modified Sum-rule model has been formulated by Bhujang et al. [19] which includes an energy-dependence in the formulation of the critical angular momentum.

2.2 Elastic scattering in the optical model

Differential cross-sections ($\frac{d\sigma}{d\Omega}(\theta)$), or angular distributions, give the angular dependence of the scattering probability. One of the most well known angular distributions is the Rutherford cross section for elastic scattering, which can be obtained via a semi-classical derivation, assuming hard-sphere scattering due to coulomb repulsion. Overlaps of the nuclear volumes at higher energies lead to nuclear interactions, and so deviations from Rutherford scattering occur. A very loose, yet useful estimate for the energy at which deviations will occur is given by the Coulomb barrier, which is the energy needed to bring the nuclei close enough for their nuclear radii to overlap.

A more accurate quantum mechanical treatment is provided by scattering theory[2]. The wave function $\psi(\mathbf{r})$ of the system of incident and scattered particles is a solution of the Schrödinger equation,

$$(\hat{T} + U(\mathbf{r}) - E)\psi(\mathbf{r}) = 0 \tag{2.10}$$

where $\hat{T}$ is the kinetic term, E the total energy and $U(\mathbf{r})$ the scattering potential, which must reflect both the Coulomb and nuclear potentials. For a central potential $U(\mathbf{r}) = U(r)$ the angular part of $\psi(\mathbf{r})$ can be factored out and the Schrödinger equation separates into angular and radial equations. The angular momentum is a constant of motion in this case, and so the wave function can be expanded in the basis of angular momentum eigenvectors, the well known spherical harmonics. The partial wave expansion is written

$$\psi(\mathbf{r}) = \sum_l \chi_l(\mathbf{r}) = \sum_l u_l(r) Y_l^m(\theta, \phi) \tag{2.11}$$

The radial wave functions are the solutions to the second order differential equations that results from the separation of variables. Two boundary conditions are needed for a solution. The boundary conditions are asymptotic. Firstly, for the wave function to be finite everywhere it must go to zero at $r = 0$. Secondly, as r becomes arbitrarily large, it must tend to the form of the sum of an incident plane wave and scattered spherical wave:

$$\psi(\mathbf{r}) \to e^{i\mathbf{k}\cdot\mathbf{r}} + f(\theta, \phi)\frac{e^{i\mathbf{k}\cdot\mathbf{r}}}{r}; \quad \text{for } r \text{ large} \tag{2.12}$$

The angular weighting $f(\theta, \phi)$ of the scattered spherical wave is referred to the scattering amplitude, and is usually only dependent on the scattering angle θ. It can be shown that the differential cross-section for elastic scattering is proportional to the norm-squared of the scattering amplitude

$$\frac{d\sigma}{d\Omega}(\theta) \propto |f(\theta)|^2 jj \tag{2.13}$$

To determine the scattering cross-section, an appropriate potential must be chosen, and the radial equation must be solved with the above-mentioned boundary conditions

[2]For a thorough introduction see chapter 3 of the textbook of Satchler [20]

to find $f(\theta)$. The choice of an appropriate potential is the important part. For elastic scattering, the nuclear part of the potential includes both a real and imaginary component, which takes into account the loss of flux to inelastic processes

$$U(r) = V(r) + iW(r) + V_C(r) \tag{2.14}$$

$V_C(r)$ is the Coulomb potential. Typical forms of $V(r)$ and $W(r)$ are the Saxon-Woods potentials. Spin-orbit and surface terms for example can also be included in the potential. The potentials are typically determined either phenomenologically (by fitting data) or by folding a given nuclear interaction over the density functions of the two interacting nuclei.

2.3 Cluster-transfer

The reaction can be treated as a completely direct transfer process followed by neutron evapouration. *Cluster-transfer* reactions use the ideas from single nucleon transfer experiments, but applied to the transfer of a cluster of nucleons. *Cluster models*, which construct single particle states for the cluster above a certain core, are useful here. An overview of Cluster models and how calculations are performed for transfer reactions is given in this chapter.

2.3.1 Cluster model

Some nuclei, particularly light ones, can be well described in terms of clustering. A ^{8}Be nucleus for example, can be described as two α-particles. ^{7}Li can be described as a triton particle above a closed α-core. The cluster model picture is contrasted with the Shell model in figure 2.3.

In the Shell model description, the unpaired proton determines the spin parity of the ^{7}Li nucleus. To describe ^{7}Li as an α-t cluster system, we must construct first the ground state, with the correct spin and parity. The quantum numbers (N, L, J) of the triton state can be with the help of the Talmi-Moshinsky transformation [21]

$$2(N-1) + L = \sum_i (2(n_i - 1) + l_i) \tag{2.15}$$

where the sum i runs over all the nucleons in the cluster, each with quantum numbers n_i, l_i. This confines the quantum numbers of the triton state

$$2N + L = 5 \tag{2.16}$$

We must recover the spin-parity of the ^{7}Li ground state such that $J = \frac{3}{2}^{-}$. The intrinsic spin of the triton is $\frac{1}{2}^{+}$, therefore the lowest angular momentum L that can couple to a value of $\frac{3}{2}$ is $L = 1$. The parities combine correctly to $(-)$ and equation 2.16 gives $N = 2$. The ground state of the triton in the Cluster model is $2p_{3/2}{}^{-}$.

The Cluster description allows for calculations to be made for cluster-transfer reactions in an analogous way to how they are performed for single nucleon transfer reactions. It has been particularly useful in the description of breakup channels, by treating breakup (emitting a cluster) as an excitation of a cluster to unbound continuum states. A general explanation of how such calculations are performed is given in the following section.

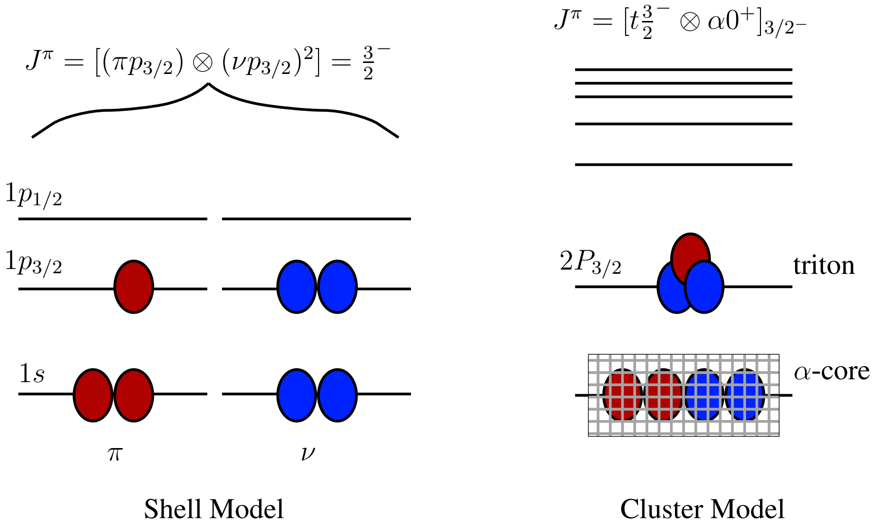

Figure 2.3: Shell and Cluster model pictures of ^{7}Li.

2.3.2 Transfer reactions

The Cluster-model allows us to extend the formalism of single nucleon transfer reactions to the transfer of a cluster. Here we consider the case of stripping in direct kinematics. A detailed derivation is available in the book of Thompson and Nunes [22]. Figure 2.4 shows the labeling of particles and the coordinate systems to describe the transfer process. Structureless particles are denoted with lowercase and composite particles with uppercase, such that the reaction $\mathrm{A} + \mathrm{b} \rightarrow \mathrm{a} + \mathrm{B}$ for the transfer of a particle or cluster x expands to

$$(\mathrm{a} + \mathrm{x}) + \mathrm{b} \rightarrow \mathrm{a} + (\mathrm{b} + \mathrm{x})$$

Two vectors are required to describe the three-body system. The internal coordinate of the composite system and the vector to the other particle are used. This results in the two coordinate systems – prior for the composite particle in the entrance channel, and post for the composite particle in the exit channel.

The composite systems in the entrance and exit channels can be described in the prior and post coordinate systems by

$$\begin{aligned} (H_A - \epsilon_A)\phi_A(\mathbf{r}) &= 0 \quad \text{where} \quad H_A = T(\mathbf{r}) + V_{ax}(\mathbf{r}) \\ (H_B - \epsilon_B)\phi_B(\mathbf{r}') &= 0 \quad \text{where} \quad H_B = T(\mathbf{r}') + V_{bx}(\mathbf{r}') \end{aligned} \tag{2.17}$$

This could be a system of a valence nucleon x, or a cluster system as described in the previous subsection. The other particles are assumed to be structureless. The total hamiltonian must include the interactions of the cores (a and b) with the cluster (x), as well as the core-core interaction $U_{ab}(\mathbf{R}_{ab})$

$$H = [T(\mathbf{r}^{(\prime)}) + T(\mathbf{R}^{(\prime)})] + V_{ax}(\mathbf{r}) + V_{bx}(\mathbf{r}') + U_{ab}(\mathbf{R}_{ab}) \tag{2.18}$$

The total kinetic energy can be expressed in either coordinate system. The expressions for the composite systems in equations 2.17 can each be substituted above to obtain post

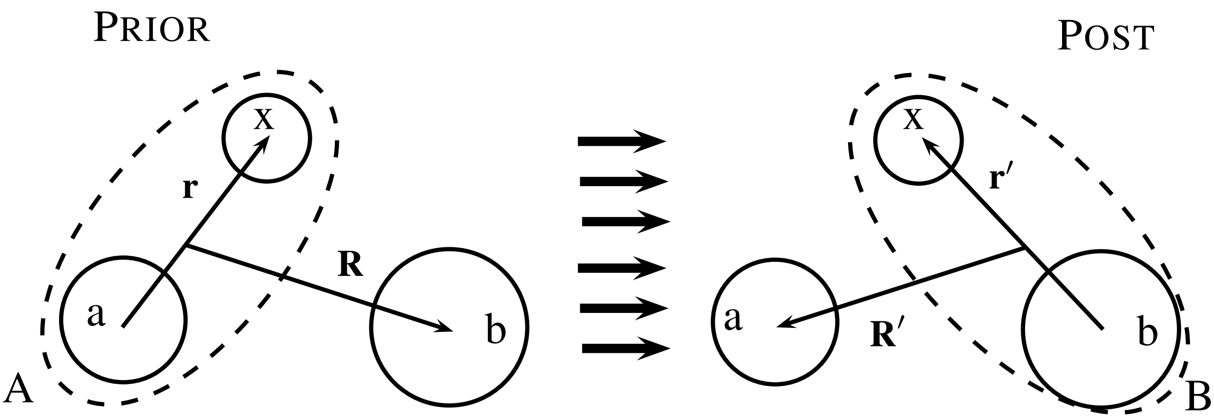

Figure 2.4: Labeling of particles and coordinate systems for massive transfer reactions. Lowercase particle indices are structureless. **R** vectors are from the center of mass of the combined systems.

and prior representations of the total Hamiltonian. Rearranging the potentials allows us to write

$$\begin{aligned} H &= H_{prior} = T(\mathbf{R}) + H_A(\mathbf{r}) + [V_{bx}(\mathbf{r}') + U_{ab}(\mathbf{R}_{ab})] \\ &= H_{post} = T(\mathbf{R}') + H_B(\mathbf{r}') + [V_{ax}(\mathbf{r}) + U_{ab}(\mathbf{R}_{ab})] \end{aligned} \tag{2.19}$$

The sum of potentials in square brackets can be separated into diagonal and off-diagonal potentials. The diagonal potentials describe the interaction of the composite particle and the other particle each picture. No mass is transferred, and so normal optical potentials can be used[3]. The diagonal potentials are resposible for the transition between bounds states in the transfer. This allows us to write:

$$\begin{aligned} H &= H_{prior} = T(\mathbf{R}) + U_{Ab}(R) + H_A(\mathbf{r}) + V_{int}(\mathbf{R}, \mathbf{r}) \\ &= H_{post} = T(\mathbf{R}') + U_{Ba}(R') + H_B(\mathbf{r}') + V'_{int}(\mathbf{R}', \mathbf{r}') \end{aligned} \tag{2.20}$$

where:

- $U_{Ab}(R)$ and $U_{Ba}(R')$ are the diagonal Optical potentials.
- $H_A(\mathbf{r})$ and $H_B(\mathbf{r}')$ are the Hamiltonians of the composite particles with bound states $\phi_A(\mathbf{r})$ and $\phi_B(\mathbf{r}')$.
- $V_{int}^{(\prime)}(\mathbf{R}^{(\prime)}, \mathbf{r}^{(\prime)})$ are the interaction potentials in each picture after formally extracting the diagonal potentials:

$$\begin{aligned} V_{int}(\mathbf{R}, \mathbf{r}) &= V_{bx}(\mathbf{r}') + [U_{ab}(R_{ab}) - U_{Ab}(R)] \\ V'_{int}(\mathbf{R}', \mathbf{r}') &= V_{ax}(\mathbf{r}) + [U_{ab}(R_{ab}) - U_{Ba}(R')] \end{aligned} \tag{2.21}$$

The above separation of potentials proves its worth when we note for example in the prior picture that the potentials describing the ab-system and Ab-system can be quite

[3]Here optical potentials are denoted with U whereas interaction potentials are denoted with V.

similar. The difference between these potentials (in square backets in equation 2.21) can therefore be very small, and so these *remnant terms* are often neglected.

With these potentials the matrix elements of the Hamiltonian can be found. The total wave-function of the system is the sum of the incident and exit channels, which can be represented in a simplified form for transfer between two states as

$$\Psi = \chi_\alpha(\mathbf{R})\phi_A(\mathbf{r}) + \chi_\beta(\mathbf{R}')\phi_B(\mathbf{r}') \tag{2.22}$$

where χ_α and χ_β are the initial and final waves. The structureless particles in the reaction are not represented in the wave-function.

This system can be solved using the coupled channel (CC) approach. For our two channel system, the projections $\langle\phi_A|\,(H-E)\,|\Psi\rangle$ and $\langle\phi_B|\,(H-E)\,|\Psi\rangle$ lead to two coupled equations for χ_α and χ_β. However, the basis states of the different composite systems or mass partitions are not necessarily orthogonal, i.e. $\langle\phi_A|\phi_B\rangle \neq 0$. Non-orthogonal terms must be treated under some approximation, for example DWBA[4]. In first order DWBA, it can be shown that these terms indeed vanish [23] which leads to the following coupled equations

$$\begin{aligned}(E-\epsilon_A-T_\alpha-U_{Ab})\tilde{\chi}_\alpha &\simeq 0\\ (E-\epsilon_B-T_\beta-U_{Ba})\tilde{\chi}_\beta &= V^{(\prime)}_{int}\,\tilde{\chi}_\alpha\end{aligned} \tag{2.23}$$

where $V^{(\prime)}_{AB}$ is the matrix element of the interaction potential in the post or prior picture and $\tilde{\chi}$ are the DWBA waves. The above equations can be solved against the same asymptotic boundary conditions of the elastic scattering case. The states of the composite system are constructed with either nucleon core couplings in the Shell model for single nucleon transfer, or with cluster-core couplings as in the Cluster model. The transition matrix elements can then be calculated, the norm-squared of which gives the differential cross section analogously to the elastic case. Of course more complicated approximations are available for more accurate calculations, but these are beyond the scope of this explanatory discussion.

The post and prior descriptions allow us some freedom in the potentials which we require in order to perform such a calculation. If all the remnant terms are included, the result must be the same in both pictures. In first order DWBA, it can be shown that the use of the post or prior interaction potentials yield the same result. For the case of cluster-transfer of ^{98}Rb on ^{7}Li, a picture should be chosen where the potentials are best known. Consider the case of triton-transfer. The results above apply, after the following substitutions

x $\Rightarrow$ triton cluster
a $\Rightarrow$ α-core
A $\Rightarrow$ ^{7}Li composite particle
b $\Rightarrow$ ^{98}Rb core
B $\Rightarrow$ ^{101}Sr composite particle

[4]Distorted Wave Born Approximation. The approximation and how it is used in such calculations is described in detail in the book of Thompson and Nunes [22]

The interaction potentials in the prior and post pictures are given by equations 2.21

$$
\begin{aligned}
V_{int} &= V_{bx}(^{98}\mathrm{Rb}, t) + [U_{ab}(\alpha, ^{98}\mathrm{Rb}) + U_{Ab}(^{7}\mathrm{Li}, ^{98}\mathrm{Rb})] \\
V'_{int} &= V_{ax}(\alpha, t) + [U_{ab}(\alpha, ^{98}\mathrm{Rb}) - U_{Ba}(^{101}\mathrm{Sr}, \alpha)]
\end{aligned} \tag{2.24}
$$

where the corresponding particles are given in the parentheses. The prior picture is a clear choice for two reasons: (1) the optical potentials of the remnant terms are more similar and (2) the α-triton binding potential is very well known, especially compared to the ^{98}Rb-triton binding potential. Again potentials can be obtained phenomenologically or by folding. The systems of equations in the methods described in this section can be solved using a specialized numerical code such as FRESCO [23] to obtain differential cross-sections.

2.4 Break-up

Breakup is the splitting of a nucleus into lighter fragments. The weakly bound ^{7}Li nucleus will readily breakup into an α-particle and a triton if it is provided the 2.5 MeV binding energy of the system. In the context of nuclear scattering, breakup can occur when the projectile nucleus interacts with a target nucleus (see figure 2.5a). Elastic breakup is the specific case where neither the fragments nor the target nucleus are excited.

Consider again ^{7}Li as an α-triton cluster system (figure 2.5b). The breakup can be understood as an inelastic excitation of the triton to unbound continuum states above the breakup threshold. For elastic breakup, all energy in the α-triton system over and above the threshold is reflected in the kinetic energies of the fragmented particles and the heavy nucleus. To account for couplings to unbound continuum states, the Continuum Discretized Coupled Channels (CDCC) approach has been devised. How calculations in this scheme are performed is described in ref. [22]. The implications of breakup in this work is discussed in section 3.3.

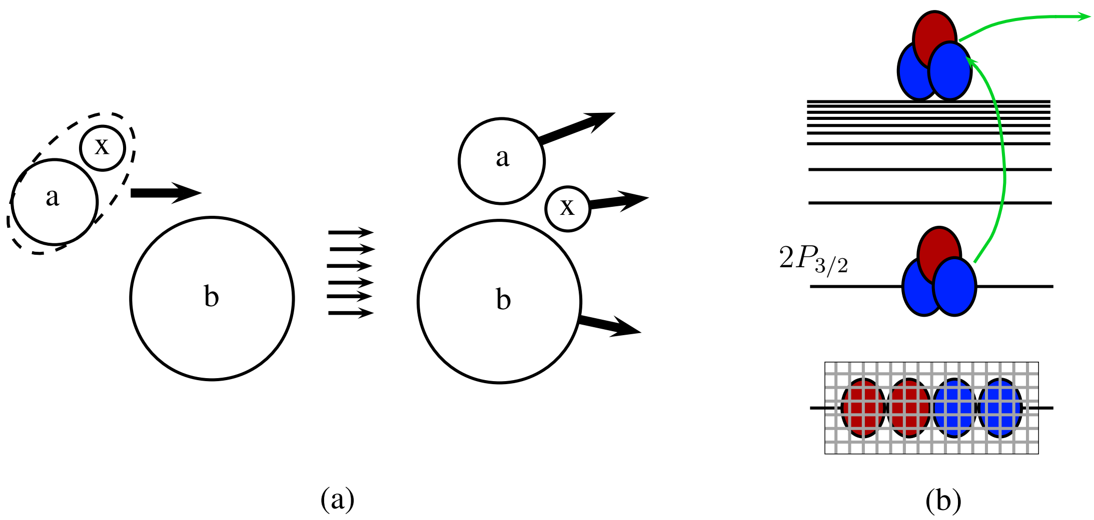

Figure 2.5: (a) Schematic of breakup. (b) Breakup of ^{7}Li as an inelastic excitation to unbound continuum states in a Cluster model.

Chapter 3

Experiment

3.1 Transfer reactions at ISOLDE

The experiment was performed at ISOLDE [6] using only part of the charged particle detector TREX[24] coupled to the Germanium γ-detector array MINIBALL [25]. In this section the experimental setup at ISOLDE is first described quite generally before the particularities of the experiment in question are presented.

3.1.1 ISOLDE

ISOLDE [6], the Isotope Separator On Line, is an experimental setup at CERN that produces a diverse range of high intensity and energy radioactive ion beams (RIBs). Beams of ions with proton number $Z = 2$ to $Z = 88$ are produced.

ISOLDE uses the Proton Synchrotron Booster (PSB) at CERN. This accelerator provides a beam of protons at 1.4 GeV at an intensity of up to 2μA [6]. The proton beam is directed onto a hot production target where fragmentation, spallation and fission reactions produce the nuclei of interest, amongst others. An ion source then ionizes the nuclei so that they can be accelerated. The choice of target and ion source depends on the particular element desired for the secondary beam. Several combinations have been developed for ISOLDE to enable the production of diverse beams. Fast extraction from the target is crucial. This is specified by the release time, which can range from 30 seconds to tenths of a second for the fasted setup.

Furthermore, there are two online mass separators with their own target-ion source setups at ISOLDE. The first, the General Purpose Separator (GPS) can provide three mass separated beams simultaneously. The second, the High Resolution Separator earns its name, providing a single beam with a mass resolving power of 5000 [6][1]. The resulting beam energy is approximately 60 keV. There are experimental installations for nuclear spectroscopy, nuclear orientation, laser spectroscopy, mass measurements, solid state physics and surface studies.

3.1.2 REX-ISOLDE

REX (Radioactive Beam Experiment) [12] is a post accelerator for ISOLDE, providing radioactive beams of higher energies up to 3.1 MeV/u. The singly ionized beam from

[1]FWHM definition of mass resolving power; $R = \frac{M}{\Delta M}$

ISOLDE is first captured and accumulated in a Penning trap, REXTRAP. A combination of an axial magnetic field and a quadrupole electric field traps ions on an epitochroidal (resembling a circular coil) trajectory. The cyclotron frequency is determined by the fields and the mass of the ion, making the trap weakly mass selective. Trapped ions are cooled by collisions with a buffer gas. The buffer gas composition and pressure are determined by the incident beam energy (60 keV) and trap size (0.9 m) to optimize accumulation efficiency of the beam ions. Normal buffer gas pressure is of the order mbar. From REXTRAP ions are extracted by lowering the potential barrier of the trap.

The next component is REXEBIS, an Electron Beam Ion Source. An intense electron beam is used to further ionize the singly ionized ions from REXTRAP by electron impact. The electron beam also creates a radial trap for the positive ions, due to the negative space charge of the electrons. Cyclindrical electrodes on the electron beam axis provide longitudinal trapping. The trapping allows a large ionization (up to bare) possible because ions are impacted repeatedly. After a breeding time of tens to hundreds of milliseconds, ions are extracted, again by lowering the potential barrier of the trap. Extraction is quick, with a measurement showing 90% of the ions extracted in 80 μs [12]. The breeding time will affect the charge state distribution of the released radioactive nuclei.

Contaminants from residual gases in REXEBIS are significant so the beam must be mass separated. But the energy spread of the highly ionized beam from REXEBIS is quite high. Therefore a Nier-type spectrometer with electric field bending to first separate the beam by energy and magnetic field bending to separate the beam by charge-mass ratio is used. Contaminants with the same charge-mass ratio cannot be separated and must be taken into account.

The separated beam is then accelerated in a linear accelerator which takes the energy up to 3 MeV/u. The accelerator line is 10 m long. A RFG accelerator takes the energy from 5 to 300 keV. The beam is then focused and rebunched in preparation for the Interdigital H-type (IH) structure which accelerates to 1.2 MeV. Three 7-gap resonators follow, and finally a 9-gap resonator. The output beam energy can be varied between 0.8 and 3.0 MeV/u by the gap resonators. The beam is then directed to the detection setup where reactions take place on a foil of a chosen material. The outgoing radiation is detected in the TREX and MINIBALL arrays (see below).

3.1.3 TREX and MINIBALL

TREX [24] ("Transfer" REX) is a Silicon particle detection setup at REX-ISOLDE developed with transfer reactions in inverse kinematics in mind. In such reactions, light particles can be emitted at a wide range of angles whilst the heavy residual nuclei tend to continue down the beamline. Large angular coverage for the detection of light charged particles is necessary. In such experiments simultaneous γ-spectroscopy is also needed. TREX was therefore designed to be compact enough to fit inside a γ-detection array such as MINIBALL (see below) and use minimal material so as not to deteriorate γ detection efficiency.

A schematic of the vacuum chamber of TREX is shown in figure 3.1a. In its complete form, the detector array consists of two box-like Si barrels forward and backwards of the target. To increase the angular coverage the ends of the barrels are closed off with CD-shaped Si detectors. The above-mentioned detectors all include a thicker rear detector for ΔE-E identification.

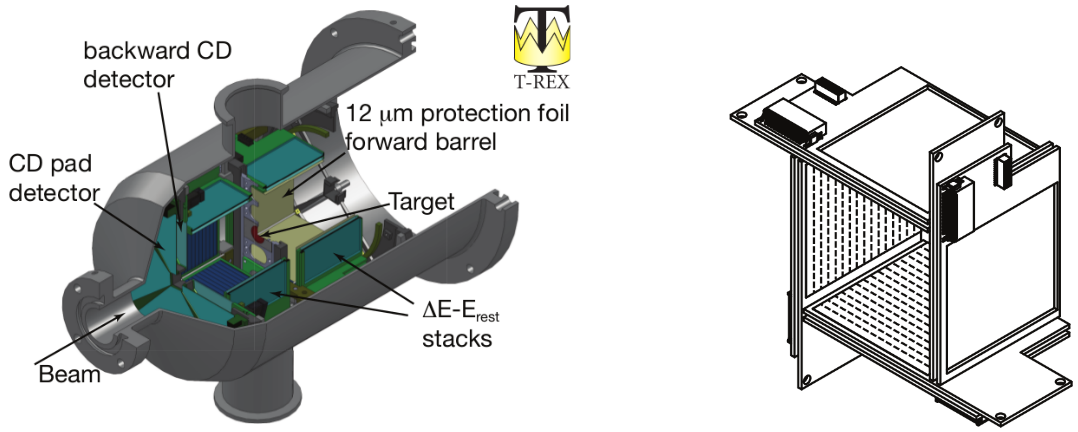

(a) (b)

Figure 3.1: (a) The TREX vacuum chamber. (b) A barrel detector of TREX, indicating the windmill-like structure with the PCBs [24].

The barrels are formed by arranging four ΔE-E detectors in a box around the beam axis at a distance of 29 mm. The ΔE detectors are 50 mm×50 mm RSSDs (Resistive Silicon Strip Detectors). RSSDs were chosen to minimize the number of readout channels (as apposed to DSSSDs, see below) and add to the compactness of the setup. The strip segmentation is 3.125 mm. Position resolution parallel to the segmentation is achieved by signal analysis and is far superior at about 0.1 mm for 5 MeV α-particles [24].

For the barrel detectors it was important to maximise angular coverage and compactness. The strips must be connected at one end to a PCB (Printed Circuit Board). Therefore a windmill structure is used (see figure 3.1b), with the segmentation perpendicular to the beam axis and the PCBs extruding from the box, maximizing angular coverage at the expense of resolution in lab angle. The E detectors at the back of each RSSD are simple Si pad detectors.

The CD detectors can be used either on their own or together with the barrel detectors. The ΔE part of the CD detectors are DSSSD's (Dual Sided Silicon Strip Detectors) with annular segmentation at the front and radial segmentation at the back for position resolution. The inner radius is 9 mm and the outer 41 mm, greater than the radius of the barrel detectors. The position resolution in the normal geometry is superior to that of the Barrel detectors.

MINIBALL [25] is a sophisticated 4π γ-detection array that is used in conjunction with TREX to detect the γ-decay of the residual nucleus. Developed for use with low intensity RIBs, detection efficiency was optimised instead of peak resolving power and maximum γ-ray multiplicity, in contrast to arrays such as Euroball. The array consists of 8 cluster detectors arranged in a spherical structure, each with 18 segments, yielding a granularity of 144 and angular coverage of 65% of 4π [26]. The segmentation allows for the determination of the position of the first interaction of the γ-ray in the detector. Pulse shape analysis and other analyses can be performed to improve the position resolution to about 1 cm for 1.3 MeV γ-rays. This is necessary for Doppler correction. The combination of TREX and MINIBALL allows for the complete reconstruction of a transfer reaction event.

3.2 Experimental Setup

The experiment was performed at the ISOLDE experimental hall at CERN. REX-ISOLDE provided a beam of ^{98}Rb at an energy of 2.85 MeV/u. The beam was available for 5 days. During the experiment, the beam intensity was estimated to be of the order of 10^5 particles per second (pps).

A 1.5 mg cm^{-2} LiF target was used. In addition to scattering on ^{7}Li, there is scattering on both fluorine and contaminant protons. This target is thicker than targets typically used at ISOLDE for transfer experiments. With the low count rates of cluster-transfer reactions, a thicker target was intended to increase the total yield. The increase comes at the price of a significant spread in energy from energy loss in the target. The 2.85 MeV/u beam of ^{98}Rb is stopped to 2.48 MeV/u mid-target and 2.11 MeV/u at the back of the target. With thin targets, energy loss is negligible, and the assumption of a mono-energetic beam at the the center of the target energy is fair. However, in this experiment, the spread of 70 MeV across the target cannot be ignored.

The full TREX setup was not used. The forward barrel and backwards CD were excluded, and the forward CD (FCD) was placed very close to the target, in the so-called "Coulex-setup". Figure 3.2 shows the geometry and dimensions of the setup.

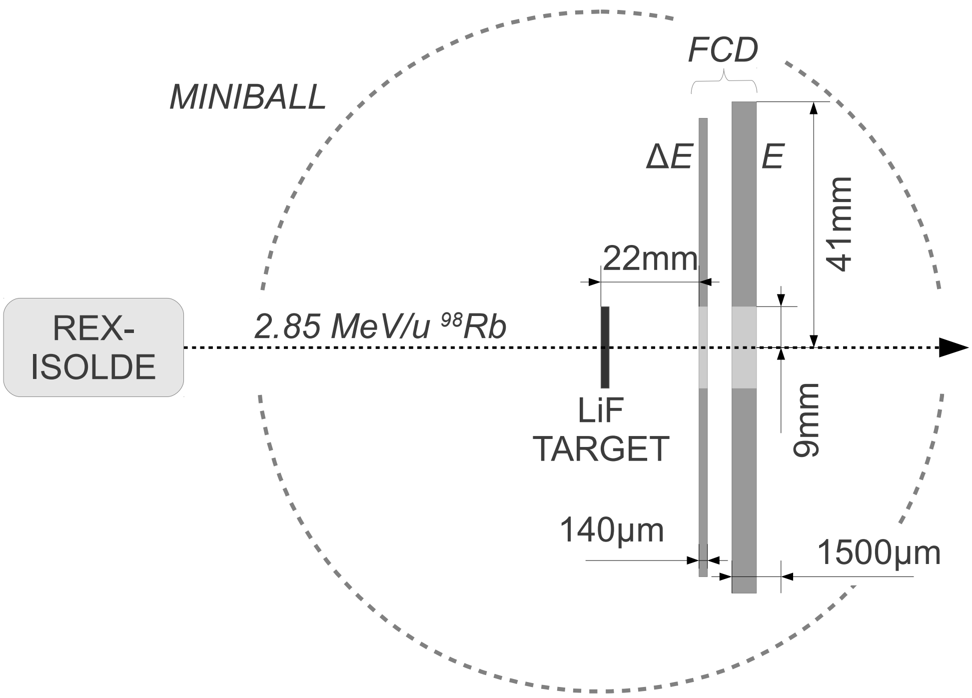

Figure 3.2: Schematic of the experimental setup with dimensions (not to scale).

The forward CD is an annular detector consisting of a segmented ΔE and unsegmented E detector, both by Micron Semiconductors [27] (designs QQQ2 and QQQ1 respectively). The CD geometries of both the ΔE and E detectors are separated into 4 quadrants, as shown in figure 3.3. The dimensions of the detectors are given in table 3.1. The detectors have aluminium dead layers of approximately 0.7 μm [24].

The ΔE-E arrangement provides both the energy and identity of a charged particle. The energy loss in the thinner front ΔE detector as a charged particle passes through together with detection of the particle's remaining energy in the E detector identifies the

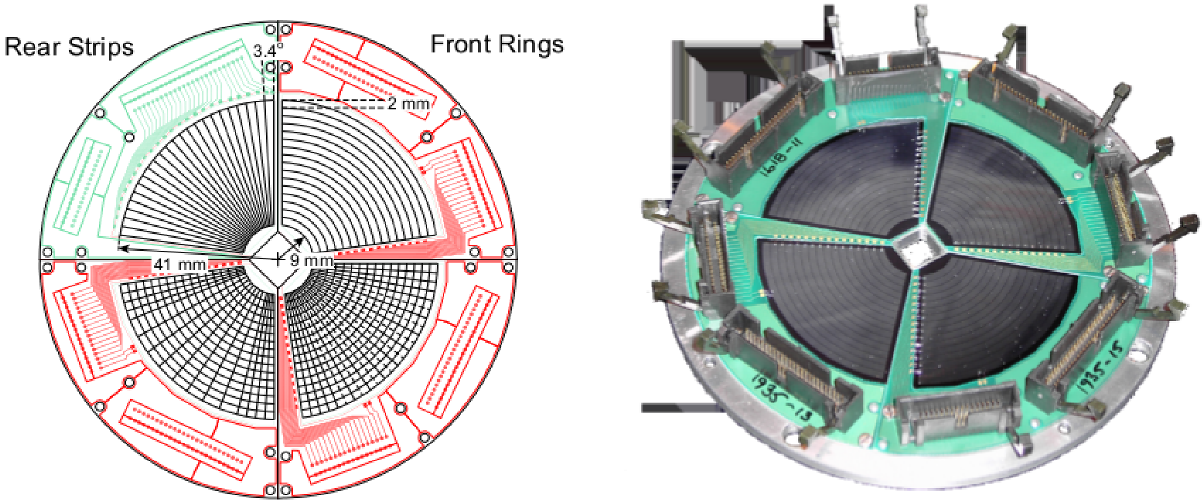

Figure 3.3: Forward CD (FCD) detector. (left) Drawing showing the different segmentations of the Si ΔE detector. (right) Photo of the front of the detector.

Detector	*Design*	*Radius*	*Quad. angle*	*Thickness*
ΔE	Micron QQQ2	9 – 41 mm	81.6°	140 μm
E	Micron QQQ1	9 – 50 mm	82°	1500 μm

Table 3.1: Dimensions of the FCD detector [24]. "Quadrant angle" refers to angle covered by each quadrant.

particle.

The ΔE detector is segmented to provide position resolution, as shown in figure 3.3 (left). The front surface is segmented into 16 rings at 2 mm intervals in radius. The rings are 1.9 mm wide in the radial direction, separated by 0.1 mm. The rear surface is segmented perpendicularly in the radial direction, into 24 strips of ϕ-angle 3.4°. The 16 inner strips are paired to reduce the number of strip readout channels down to 16.

Figure 3.3 (right) shows the readouts on the detector frame. The four quadrants, each with 32-fold segmentation, lead to 128 channels from the FCD ΔE alone. The detector is normally part of the TREX setup, which would include another CD and two barrels, so the number of readout channels had to be minimized for both space and cost economy. The 128 channels from the FCD ΔE are therefore encoded into fewer channels using a multiplexer. Four Mesytec MUX-32 multiplexers each with 32 input channels were used for this purpose.

Each multiplexer detects up to two simultaneous signals from the 32 connected detector segments, sending a reject signal if more than two arrive within a time window of 50ns [28]. Because a particle should register a signal in both a ring and a strip as it passes through a quadrant, multiplexers are connected to either rings or strips.

The input channel of a signal, i.e. ring/strip number, is encoded into one channel, and the signal itself into another. Adding two more such channels for the second hit signal and a global timing signal gives a total of 5 output channels from the multiplexer for each quadrant of 16 rings or strips. The 128 channels from the FCD ΔE are reduced to 40.

The gains of the detectors were set for a full-scale range of approximately 30 MeV. The data was recorded in runs of 2 hours, over the beam time of 5 days. Accounting for interruptions of the beam, the measuring time is estimated at around 80 hours.

3.3 Observed reaction channels

Though the beam delivered by REX-ISOLDE was tuned to ^{98}Rb, there was a large amount of contaminant. Firstly, ^{98}Rb has a short half life of 102 ms, β-decaying to ^{98}Sr. With the acceleration time of REX a few hundred milliseconds, one can expect a comparable amount of ^{98}Sr in the beam. Secondly, an isomer of ^{98}Rb has been observed at 270 keV. The population of this isomer is unknown. Finally, there is inevitably a small number of contaminant nuclei from the isotope production. The determination of the concentration of ^{98}Sr in the beam remains an unsolved problem[2].

Reactions on both ^{98}Rb and ^{98}Sr are therefore observed. In this work we are concerned with determining the magnitude of the cluster-transfer cross-sections. Differences in structure between these two nuclei are not expected, and so we expect the cross-sections to be much the same for both. The beam composition is therefore safely ignored.

Concerning the target of LiF, we observe unwanted scattering not only of the fluorine, but also from contaminant protons. The beam energy of 2.85 MeV/u is well below the Coulomb barriers[3] for these nuclei, and so only Rutherford-like elastic scattering is observed. The elastic scattering channels are shown in table 3.2 with their respective Coulomb barriers. For the elastic scattering channel of interest, ^{98}Rb on ^{7}Li, we are approximately at the Coulomb barrier. The strongest elastic scattering channel will be on fluorine, followed by ^{7}Li.

Elastic Channel	$E_{\mathbf{cm}}$	B_c
$^{98}\mathrm{Rb} + ^{7}\mathrm{Li}$	16.2	16.6
$^{98}\mathrm{Rb} + p$	2.45	6.55
$^{98}\mathrm{Rb} + ^{19}\mathrm{F}$	39.5	45.3

Table 3.2: Elastic scattering channels: center of mass energy at mid-target beam energy of 243 MeV ^{98}Rb and Coulomb barrier calculated in the Bass model [29].

Cluster transfer occurs with a much lower cross-section than elastic scattering. The α- and triton-transfer channels are the focus of this work. They are observed by the detection of tritons and α-particles respectively. It is useful to consider the energetics of these reactions briefly, as the excitation energy of the residual nucleus determines the energy of the α-particles and tritons that are detected.

In transfer reactions in general, there is an optimum Q-value ($Q = Q_{\mathrm{gg}} - E_{\mathrm{x}}$) for a transfer channel, which determines how much of the energy in the incident channel

[2]One could propose look to the γ-rays from the β-decay chain, but the intensities of the β-decay channels are not well-known in this very exotic region.

[3]The Coulomb barrier is a very conservative indication of whether the nuclear volumes can approach close enough for a nuclear reaction

remains to be distributed amongst the two outgoing particles (two-body kinematics). This optimum Q-value can be estimated with semi-classical models. The model of Brink [30] for example derives optimum conditions for nucleon transfer by assuming the smooth transfer of a nucleon from its orbital in the projectile to a specified orbital in the residual nucleus, by semi-classically matching the orbital and total angular momenta. This model can be extended to massive transfer of clusters for which the excitation energy of the residual nucleus is typically very high.

For the case of ^{98}Rb on ^{7}Li the optimum excitation energies of the residual nuclei ($E_{\mathrm{x}} = Q_{\mathrm{gg}} - Q$) were calculated with the model of Brink [30] by averaging over transfer to states with $l = 0$ to $l = 5$ in the the residual nucleus[4]. The results of the calculation are shown in table 3.3. The ground state Q-values are also shown, and are very high because of the weak binding of ^{7}Li. The residual nuclei are produced at very high excitation, which means that the outgoing α-particles and tritons will have somewhat lower energy.

Transfer Channel	$Q_{\mathbf{gg}}$	Q^{opt}	$E_{\mathbf{x}}^{\mathrm{opt}}$
$^{98}\mathrm{Rb}(^{7}\mathrm{Li}, \alpha)^{101}\mathrm{Sr}$	13.7	-6.0	19.7
$^{98}\mathrm{Rb}(^{7}\mathrm{Li}, \mathrm{t})^{102}\mathrm{Y}$	7.6	-11.8	19.4

Table 3.3: Transfer channels of interest. The ground-state Q-value, optimum Q-value and optimum excitation energy $E_{\mathrm{x}}^{\mathrm{opt}}$ (see text) are given in units of MeV.

Unfortunately, the α-particles and tritons that identify the cluster-transfer channels of interest, also come from the breakup of the weakly bound ^{7}Li nucleus. In elastic breakup the energy in the entrance channel (beam energy) less the binding energy of the light nucleus is divided as kinetic energy amongst the three outgoing particles such that energy and momentum are conserved (three body kinematics). The kinematics of the tritons and α-particles from massive transfer (two-body) and breakup (three-body), with the above energy considerations, turn out to be very similar for our system of ^{98}Rb on ^{7}Li. For this reason it is not possible to separate the particles arising from breakup from those resulting from transfer through particle detection. The contribution of breakup to the detected particles must be estimated by looking at particle-γ anti-coincidence.

Other massive transfer reactions are possible, namely neutron-transfer (^{7}Li,^{6}Li), proton-transfer (^{7}Li,^{6}He), ^{5}He-transfer (^{7}Li,d) and ^{6}Li-transfer (^{7}Li,n). These channels are expected to be very weak. Due to the comparative strength of the elastic ^{7}Li channel, the much weaker and kinematically similar single neutron transfer channel (^{7}Li, ^{6}Li) cannot be separated.

The outgoing particles of the above-mentioned reactions were detected in the FCD detector. The analysis of the data, focusing on the elastic scattering of ^{7}Li and the transfer channels of interest, is presented in the following chapter.

[4]Work of S. Bottoni.

Chapter 4

Analysis

Introduction

Analysis of the particles detected in the FCD formed most of the work done for this thesis. Calibration and particle identification were followed by careful treatment of the elastically scattered ^{7}Li, which led to a scaling factor for differential cross-sections of the other particles. Another result that followed from the analysis of the elastic scattering is the average beam intensity. This chapter discusses the analysis in detail. The results are discussed in Chapter 5.

Our setup made necessary careful considerations of the approximations that are made in each step of the analysis. With the FCD very close to the thicker than usual target, geometrical and energy loss considerations were necessary. For this reason, the geometry and transformations are calculated in the analysis, and described in some detail. These steps are commonly performed using a comprehensive simulation. For our setup, a full GEANT4 [31] simulation of the TREX+MINIBALL setup was adapted by F. Flavigny. The analysis was performed both analytically and with the simulation to demonstrate the correspondence and confirm what is often taken for granted.

Unless otherwise mentioned, all analysis code was written in C++ using the ROOT framework. Throughout the analysis, there was a need to calculate energy losses. For quick calculations, LISE++ [32] was used. For lengthier simulations an existing C++ implementation of the ZBL (Ziegler, Biersack and Littmark) semi-empirical model [33] was used.

4.1 Calibration of CD detector

The first step in the analysis was to unpack and calibrate the data from the FCD. As mentioned in section 3.2, the signals from the FCD ΔE rings and strips are multiplexed. In the multiplexing, the 16 signals from the rings or strips of a quadrant are reduced to 5, allowing for a hit multiplicity of 2. Two channels are reserved for the segment number of the first and second hits. This is encoded in a garden-hedge-like spectrum with 16 (ideally) well separated peaks (see figure 4.1 left). These spectra were fitted and calibrated to assign each event in the data with a ring and strip number. Note that this can be done without even considering the energy.

The muliplexing units were misbehaving during the experiment, with some showing

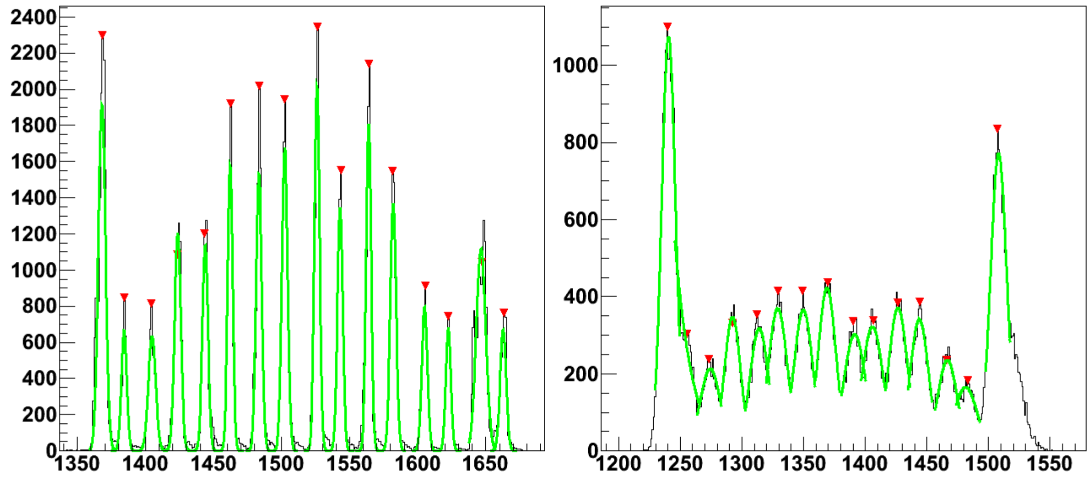

Figure 4.1: Example of good (left) and bad (right) position spectra for demultiplexing.

considerable noise, as can been seen in figure 4.1 (right). Existing code was not able to treat such cases, so a more rugged (and simpler) demultiplexing procedure was developed. The 16 peaks were fitted as best possible. The mean values were then used to calculate the midpoints between the peaks, which were then used to define windows for each peak. Events were allocated a ring/strip number using these windows.

Walk was also noticed in one of the multiplexers. A jump in the position spectra over the course of a few hours could be seen in the data well into the measuring time. This was dealt with by using two different calibrations.

A strong loss of counts was seen in the strip detectors. Events with valid ring signals, were not being registered in a strip detector. Strangely enough, these losses were seen to be pronounced for detection of Li. Fortunately, the strip signal is not needed in the analysis because of the symmetry of the scattering problem. The source of these losses could not be explained and were attributed to misbehaving electronics. Care should be taken in future experiments if they plan to utilize the ϕ-angle information from the strips.

The second calibration step was the energy calibration of the ΔE ring/strip detectors. A separate calibration was required for each ring and strip. Before the experiment measurements were taken using a mixed α-calibration source in the target frame. The source emitted alpha's with four strong lines between 3-6 MeV. Gaussian fits were used to extract the calibrations.

At this energy, the energy loss in the 0.7 μm Al dead layer in front of the detector can be significant, especially with the FCD positioned so close to the target. At wide angles towards outer rings – where the effective thickness is much larger – almost 10% of the incident energy can be lost in the dead layer. The energy of each α line after the dead layer was calculated for each ring and used in the energy calibration. The E detectors were calibrated by placing the α-source at the rear of the FCD.

Such care was taken in the analysis to ensure good calibration, because the full-scale range of the detectors were approximately 30 MeV. A small error in the calibration in the 3-6 MeV range blows up at higher energies. Segments with very poor energy resolution were treated carefully, and watched throughout the analysis or excluded entirely.

4.2 Identification of particles

Particle detection typically relies on the energy loss of charged particles as they pass through the detector material. In the case of Si semiconductor detectors, the energy lost by the particles to the medium creates a proportional number electron hole pairs. The electrical signal collected from the medium is in turn proportional to the energy deposited by the particle. In thicker detectors, where the particle is stopped, the signal is proportional to initial energy of the particle.

The Bethe-Bloch equation gives the most important proportionalities of the specific energy loss of a charged particle:

$$\left\langle \frac{dE}{dx} \right\rangle \propto \frac{z^2 M}{E} \tag{4.1}$$

where z is the atomic number of the charged particle, E its energy and M its mass. Heavier, lower energy particles will be stopped more quickly. From equation 4.1 we see that particles are identified if both the energy and specific energy loss are known. To this end, combination of a thin ΔE detector to measure energy lost over a short distance and a thick E detector to measure the remaining energy is used.

Figure 4.2 shows how different particles are identified by their energy-dependent energy loss. Identified particles appearing on the banana-shaped curves off the diagonal are said to have "punched-through" the ΔE detector[1]. Particles that do not have enough energy to penetrate the ΔE detector lie on the diagonal and cannot be identified in this way. Elastic ^{7}Li, with the largest energy and energy loss, is clearly identified. Note that the events identified as ^{7}Li may also contain ^{6}Li. The α-particles and tritons come from the triton- and α-transfer reaction channels respectively with a contribution from the elastic breakup of ^{7}Li. Deuterons and ^{6}He can be faintly observed, corresponding to the transfer of ^{5}He and a proton respectively. The large number of protons comes from the elastic scattering of contaminants.

The energy loss ΔE depends on the thickness of the ΔE detector. The effective thickness increases towards outer rings, and so each ring should be treated separately. In order to systematically separate the different particles, energy vs enery loss curves were simulated for each ring and for each particle. The lower limit was calculated using the effective thickness of the ΔE detector at the bottom of the ring, and the upper limit was calculated with the effective thickness at the top. This calculation doesn't consider energy resolution or straggling and therefore led to windows which were too narrow. A constant was added and subtracted to the upper and lower curves respectively to widen the windows to include all the particles. Examples of these particle identification splines can be seen for ^{7}Li in figure 4.6.

Unfortunately the full-scale range of the detectors were too low to include the punch-through of the lithium curve. This caused great difficulty in determining the number detected ^{7}Li particles. Treatment of this problem is discussed in section 4.3.

Another way to separate different particles in a scattering experiment is to look at the kinematics. Conservation of momentum in a two body collision relates the energy E of

[1]Similarly, the minimum energy needed for a particle to pass through the ΔE detector to reach the E detector is called the "punch-through energy".

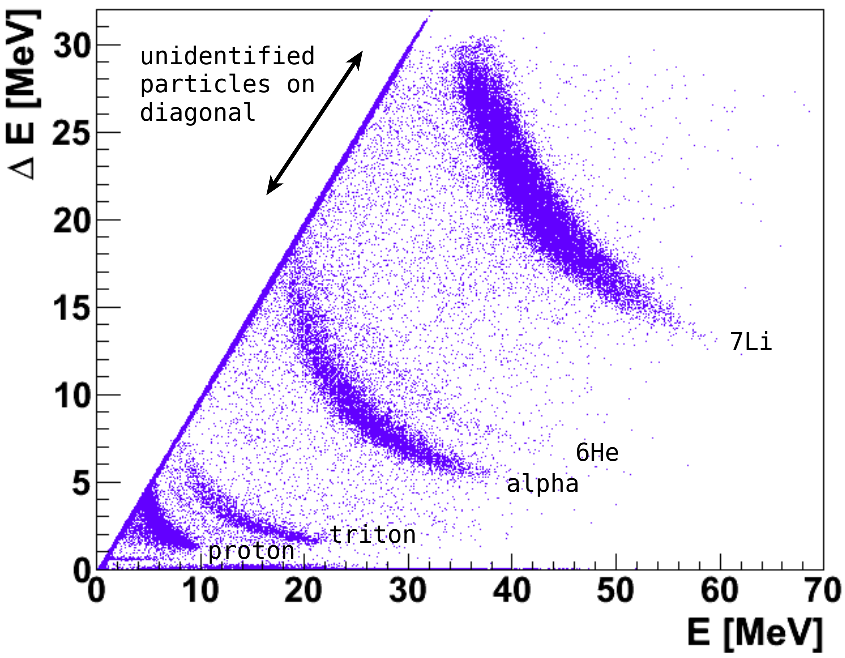

Figure 4.2: ΔE-E matrix including all quadrants and rings.

the scattered particle to the scattering angle θ. Figures 4.3 shows the energy of identified particles plotted separately against the lab angle. Figure 4.4 shows all identified particles plotted together, including unidentified particles that do not punch through the ΔE detector (found on the diagonal in figure 4.2). A continuous spread in angle is obtained by randomizing the position of a hit uniformly across the surface of the fired ring.

Given the beam energy and the masses of the particles in the entrance and exit channels, and assuming an excitation energy of the residual nucleus, $E(\theta)$ *kinematic lines* can be calculated. In practice the energy loss before and after scattering complicate the problem significantly, especially when the target is thick. The position where the scattering took place in the target is unknown. Therefore the energy before scattering is not known, and ranges between the energy at the front of the target (279 MeV) to the energy at the back of the target (207 MeV). Furthermore, the energy loss of the scattered particle after the interaction can not be calculated without knowledge of the interaction position.

A mid-target approximation is used, making the assumption that the interaction takes place at the center of the target. This allows for a single beam energy of 243 MeV (mid-target) to be used. To account for energy loss of the scattered particle in the rear half of the target under the above approximation, energy to energy loss curves are calculated for each particle. Each ring was treated separately because of the different effective thicknesses of the half target.

The final step in the calculating of the kinematic lines is to assume excitation energies. For the case of elastic scattering, the excitation energy is zero. An excitation energy was assumed for the transfer channels, to fit the calculated kinematic lines to the data. Calculated kinematic lines are shown in the $E(\theta)$ plots in black. The red curves include energy loss of the scattered particle in the target. The excitation energies are given for each reaction in figure 4.3, and are found to be more or less consistent with the semi-classical calculations of the optimal Q-value (table 3.3).

The data points are widely spread about the calculated kinematic lines because the

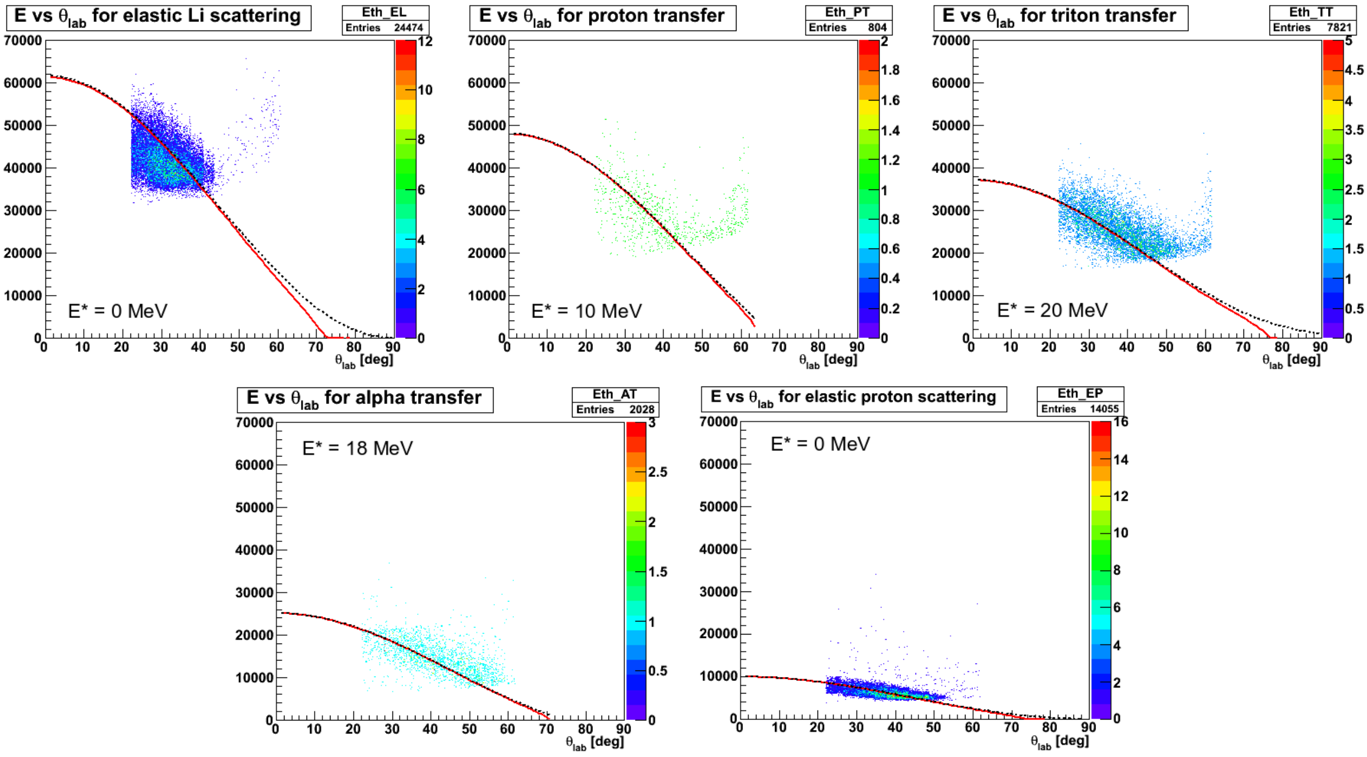

Figure 4.3: E vs θ_{lab} for all identified scattered particles. The curves (kinematic lines) are calculated from two-body kinematics, assuming an excitation energy of the residual nucleus (E^*). Red curves include energy loss in the target.

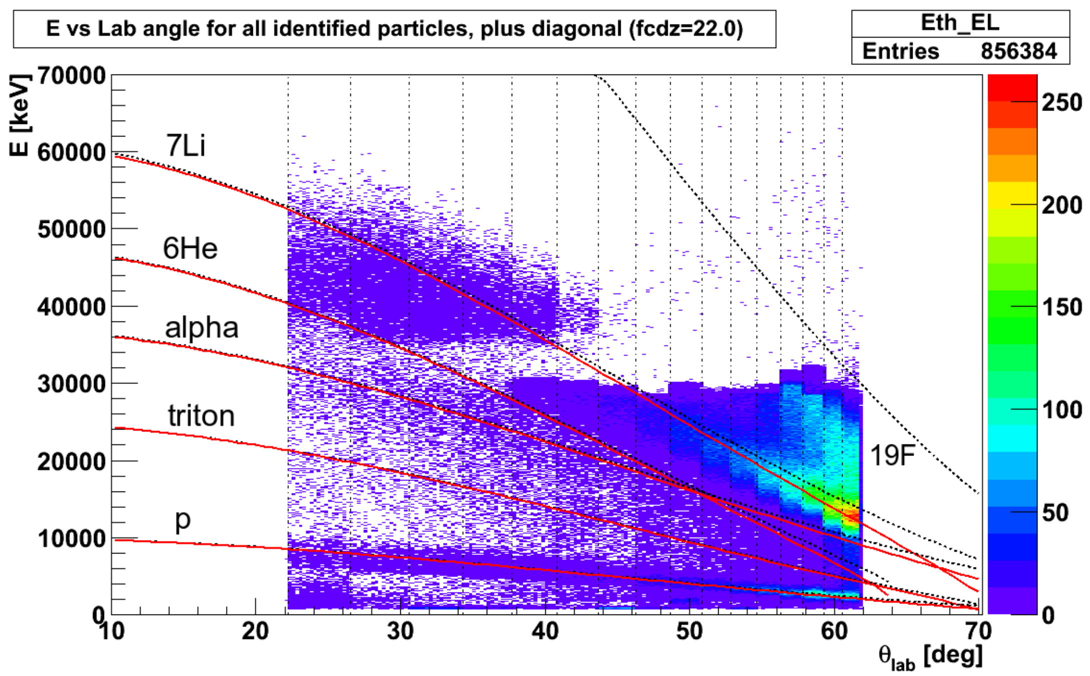

Figure 4.4: E vs θ_{lab} plot showing calculated kinematic lines. All identified particles from figure 4.3 as well as particles that do not punch through (on the diagonal of figure 4.2) are included. Fluorine can be seen at the highest energy, and only enters at large angles.

significant energy loss in the target. The beam energy ranges from 207 MeV to 279 MeV through the target – a spread of 70 MeV. The reaction cross-sections could change significantly over this interval. The Rutherford cross-section for example, has almost doubled by the back of the target, favouring lower energy scattering. A better average beam energy would be weighted by the cross-section, though this is not practical when the cross-sections are what we are trying to determine. The mid-target approximation will perform well for the calculation of kinematic lines when the target is thin and/or the cross-section for the reaction is slowly varying with energy.

The uniform smearing of the hit position is, for similar reasons, far from the truth, and shows discrete steps in figure 4.4, where the anglular ranges of the rings are plotted as vertical lines. The spread in beam energy from energy loss leads to a distribution that would be better described as a spreading perpendicular to the kinematic line calculated mid-target. This does not pose a problem when the angular range of rings is small, but in the current case where the FCD is so close to the target, the smearing is only of aesthetic use.

The position of the FCD detector was not known exactly. This number is crucial in the analysis, and therefore needed to be confirmed. The kinematic lines of the elastic ^{7}Li and p were used to fit the correct distance. By repeating the analysis needed to produce figure 4.4 for distances between 18 and 25 mm, a distance of 22 mm was found to show the best agreement between the measured elastic scattering data and the calculated kinematic lines. This value was accepted for all analysis.

With regards to particle identification, two things are evident from the $E(\theta)$ plot in figure 4.4. Firstly, the comparative strength of the elastic scattering channels compared to the transfer channels is clear, with a cross-section increasing towards 90°, in agreement with the Rutherford cross-section. ^{7}Li that has not punched through the ΔE can be identified on the diagonal because of this. Secondly, a broad line corresponding to fluorine can be noticed. The kinematic line for fluorine was calculated and is shown in figure 4.4, but energy loss was not considered. Fluorine is well separated from the ^{7}Li up until the outermost rings. Finally, the gap in the data where ^{7}Li punches through is evident between 30-40 MeV. The extraction of the number of counts of ^{7}Li is discussed in the following section.

4.3 Determining the number of counts per ring

In order to extract the differential cross-section of the elastic channel, the number of ^{7}Li particles detected in each ring must be known. ΔE-E particle identification is only useful when the particles punch through the ΔE detector. ^{7}Li particles that stop in the ΔE detector must be counted in another way.

Towards larger scattering angles, the energy of scattered ^{7}Li decreases. At the same time the effective thickness of the ΔE detector increases. By the third ring, some of the ^{7}Li are already stopped in the ΔE detector (see figure 4.6 in the appendix). Because of the strength of the elastic scattering, ^{7}Li particles that do not punch through can still be counted by fitting the energy spectrum of each ring. These 16 spectra correspond to the 16 vertical slices in figure 4.4 projected onto the energy axis. Figure 4.5 shows an example of such a spectrum – simply the *energy spectrum* measured by a ring. The background

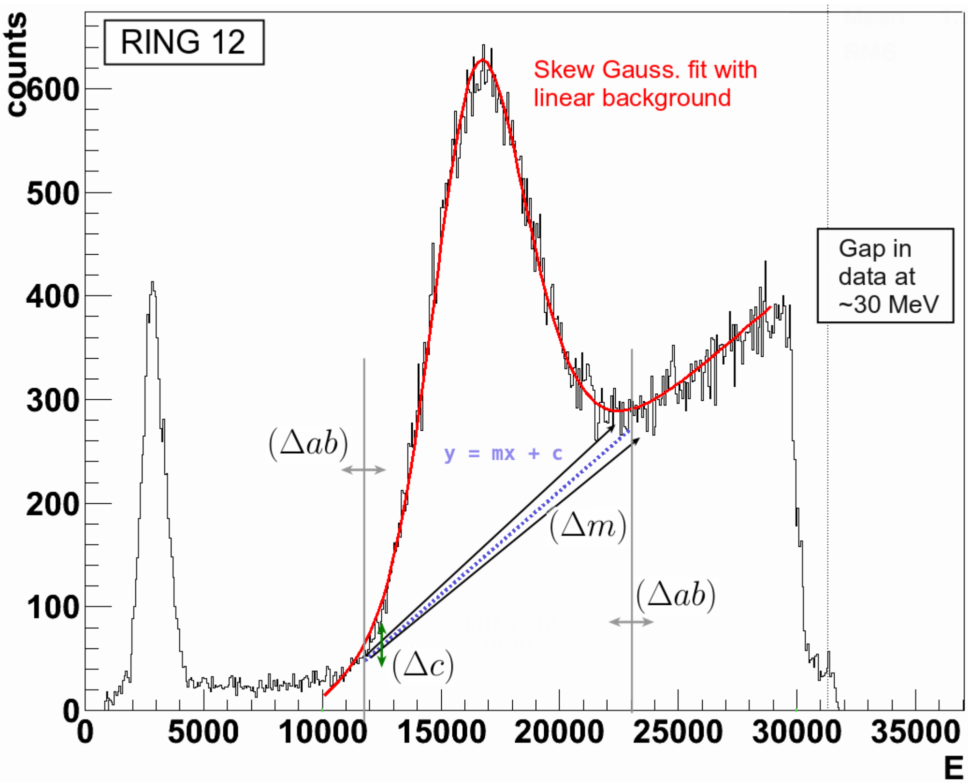

Figure 4.5: Fitting procedure of the energy spectra to extract the number of elastically scattered ^{7}Li7.

above which the ^{7}Li peak sits is from scattered fluorine.

The peak corresponding to ^{7}Li has a non-trivial shape. The spectrum represents the integral of scattered particles over the angular range of the detector. Due to energy loss in the target, scattering occurs at a wide range of energies. As discussed in the previous section, the spread in $E(\theta)$ that results would be better described by a distribution perpendicular to the kinematic line at the mid-target energy. The measured spectrum is a projection of this distribution in $E(\theta)$ onto the energy axis. The shape of this projection therefore depends on the gradient of the mid-target kinematic line. The result is a skew peak, with a shape that changes with angle. For this reason, the first attempts to fit the peak with a skew Gaussian function (with linear background) had limited success. A simpler approach turned out to be more reliable. A linear background was fitted and subtracted from the integrated counts in the peak. The error on the background was estimated by hand, by adjusting the parameters manually up to the limits where the line clearly misrepresented the data. This yielded conservative absolute errors in the gradient (Δm) and intercept (Δc). A constant error in the integration limits (Δab) was also assumed. The above errors were transformed into absolute errors on the integral, and combined quadratically to give a final error on the number of counts. It is not ideal to perform analysis in such a subjective way, but with the complexity of the peak shape and the problem of missing data due to the insufficient gain on the detectors, fitting routines were unsuccessful.

Returning to the problem of lost counts of ^{7}Li – this made many of the spectra unuseable. The consequences can be seen in figure 4.6. The two inner-most rings (0-1) can be used because all the ^{7}Li punches through. These rings do not need to be fitted. The

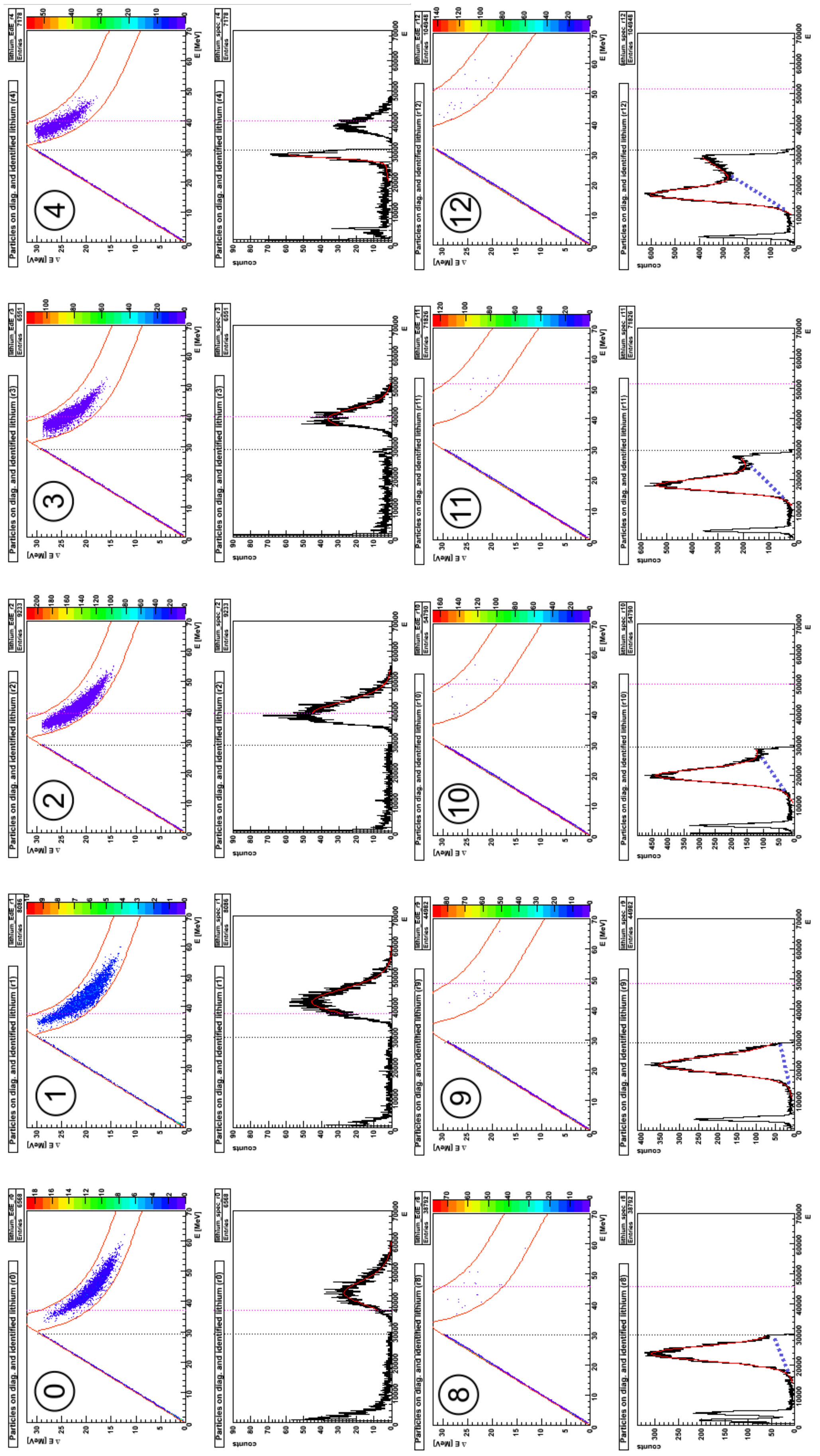

Figure 4.6: Ring by ring ΔE-E matrices with their corresponding energy spectra. Rings 0-4 and 8-12 are shown to emphasize where the ^{7}Li data is cut.

maximum energy deposited by ^{7}Li in the ΔE detector can exceed the energy range of the detector for rings 2-7. The problem is worsened by the large spread in energy. Counts can be lost from the leading or trailing edge of the ^{7}Li peak, which can be seen as sharp cut-offs in figure 4.6. Another way to visualize at which angles we lose counts is to consider the $E(\theta)$ plot in figure 4.4. The hole in the data at 30-49 MeV clearly effects many rings. In total, only 10 rings could be used for ^{7}Li. The elastically scattered protons, which didn't suffer from this loss of counts, were analyzed with the same procedure as a check of the method.

Particles from the transfer channels (α, t and ^{6}He) are lighter than ^{7}Li, and have a lower atomic number. They are therefore more penetrating than the ^{7}Li, and punch through the ΔE detector up to larger scattering angles. At wide enough angles, where kinematics result in lower energy and geometry in a thicker ΔE detector, these particles will however be stopped. The cross sections for transfer reactions are too low to enable the fitting of events in the energy spectra, therefore only ΔE-E identified data can be used. For tritons only the inner 9 rings could be used, for α-particles the inner 5 and for ^{6}He the inner 4.

4.4 Geometry and efficiency

The annular detector consists of 4 separated quadrants each with 16 rings. Due to the azimuthal symmetry of the arrangement, the rings of the quadrants can be treated as one. The result is 16 intervals i in polar angle, $\Delta\theta_i$, and in solid angle, $\Delta\Omega_i$, corresponding to complete rings ($\phi \in [0, 2\pi]$). These ring angles θ are defined from a point at the center of the target to the inner and outer radii of the rings. In this picture, the gaps between quadrants are ignored, and must therefore be included as a geometrical efficiency.

The efficiency is non-trivial to interpret. The beam has a finite spot size, and so each ring in reality includes a range of angles greater than that defined by $\Delta\theta_i$ (which treats the target as a point source). To better understand this effect, calculations were performed assuming a gaussian beam profile with a finite width. Firstly, the scattering angle ϑ must be defined separately from the angles θ which are measured from the center of the target (under the assumption of a point source). The experimentally accessible angle is θ; this must be related to the scattering angle ϑ.

Assume a gaussian beam profile with a certain width incident on the target as shown in figure 4.7. The blue areas indicate a ring-like detector area, which could be either a ring, or a combination of rings. For a certain scattering angle ϑ, the coordinates on the target, $x_0(\vartheta)$ and $x_1(\vartheta)$, which bound trajectories that will reach the detector area, can be calculated with simple trigonometric expressions.

The intensity of particles scattered through an angle ϑ from a position $x \in [x_0, x_1]$ in the target is proportional to the intensity of the beam at x. Therefore integrating the normalized Gaussian beam profile between the limits $x_0(\vartheta)$ and $x_1(\vartheta)$ yields the fraction of particles that have scattered with an angle ϑ that will reach the detector area:

$$\varepsilon(\vartheta) = \frac{1}{c\sqrt{2\pi}} \int_{x_0(\vartheta)}^{x_1(\vartheta)} dx \ \exp\left(\frac{-x^2}{2c^2}\right) \tag{4.2}$$

$\varepsilon(\vartheta)$ will be referred to as the scattering angle efficiency or ϑ-efficiency. The parameter c is related to the FWHM of the beam.

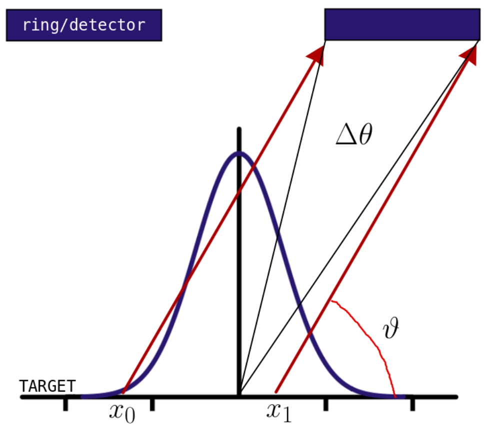

Figure 4.7: Schematic of the calculation of the trajectories that reach a detector at an angle ϑ. x_0 and x_1 are the integration limits that depend on the angle ϑ.

Figure 4.8a shows the resulting ϑ-efficiency profiles for each ring separately, including segmentation. Repeating the calculation, treating the 16 rings as one solid detector area, yields an agreeable result, equal to the sum of the efficiencies of the 16 rings. Clearly the range of scattering angles that are detected in a ring is much larger than the angular coverage of the ring. Also, it is possible for some scattering angles to be detected in different rings. The integral of the curves over ϑ are equal to $\Delta\theta_i$ and are therein related to the solid angle.

Experimentally, our knowledge of the scattering angle is limited by the geometry of the rings and so in the analysis that follows, it is necessary to assign an average angle to a ring. The vertical lines in figure 4.8a correspond to the θ-angle at the center of each ring, θ_i. Simple geometrical considerations reveal that the integral in eq. 4.2 will always be maximal when $\vartheta = \theta_i$. The curves are almost symmetric, therefore the angle at the center of the ring is a good approximation of the scattering angle. This definition however leads to asymmetric errors in theta. The average between the inner and outer angles of a ring differs by less than 1%, and can therefore also be used. The error on the angle is approximated by the range of the ring $\Delta\theta_i$ because of the clear correspondence to the geometry of the setup.

In the GEANT4 simulation, beam width, target thickness and dead spots in the detector are included. Events are simulated, and so the exact scattering angle ϑ is known. The same curve as calculated above – the fraction of particles that scatter with an angle ϑ that are detected – can be extracted from the simulation. This is quantitatively more reliable than the calculation performed above, as it includes the full geometry of the FCD. The simulated $\varepsilon(\vartheta)$ curve is shown in figure 4.8b, and agrees with the calculated curve. The drop in height is a direct consequence of the dead spots between the detector quadrants. From this curve efficiency corrections can be extracted.

The top of the simulated curve is flat, and corresponds to a rescaling of all the calculated curves. The efficiency factor ϵ must therefore be *the same* for all rings. This number is most easily extracted from the flat section of the curve, and was found to be

$$\epsilon = 0.86 \pm 0.01$$

The number scattered particles is then related to the number of particles detected in a

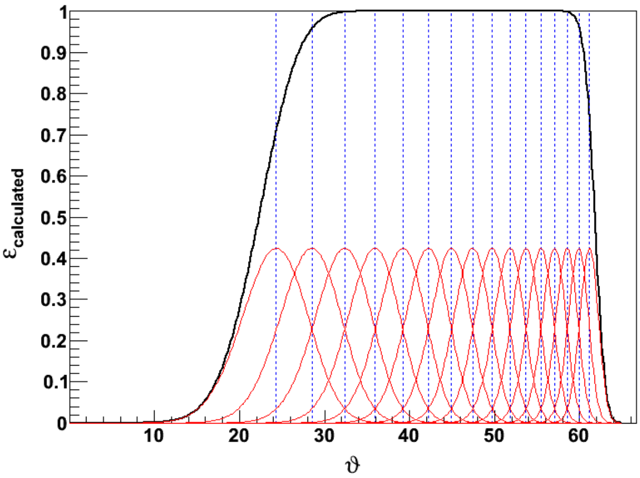

(a)

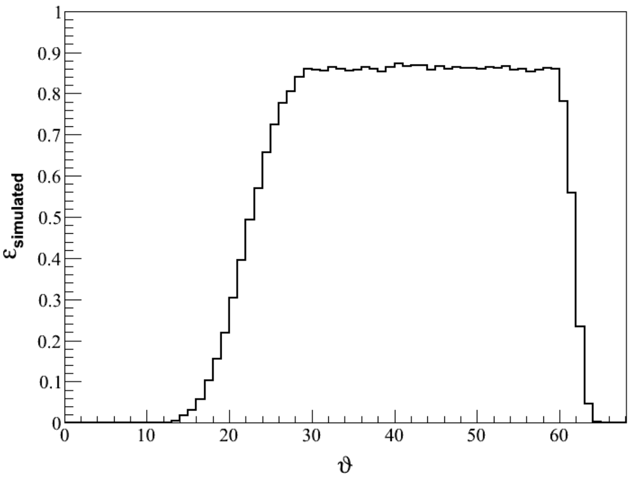

(b)

Figure 4.8: (a) Calculated and (b) simulated ϑ-efficiencies of the annular detector at a distance of 22 mm from the target (*Simulation courtesy of F. Flavigny*). In figure (a) the contributions of each ring to the total ϑ-efficiency are shown in red. The angles at the center of the rings are shown in blue.

ring i:

$$N_i = N_{D,i}/\epsilon \tag{4.3}$$

In summary, the difference between the ϑ-angles in the above figures and the θ-angles defining the geometry of the ring is subtle yet important. It is incorrect to simply sample the simulated curve at ring angle θ_i as this ϑ-efficiency has an entirely different meaning, as can be seen at the edges of the detector. When the FCD is far enough from the target, the behaviour at the fringes is sharper, and so this distinction is often overlooked. It is also important to note that we are integrating a range of scattering angles in each ring over a range wider than the opening angle ($\Delta\theta_i$) of the ring.

4.5 Scattering cross sections in the CM frame

The number of particles detected in an element of solid angle $\Delta\Omega$ is expressed in terms of the differential cross section $\frac{d\sigma}{d\Omega}$ by:

$$N_{\Delta\Omega} = N_0 n_t \frac{d\sigma}{d\Omega} \Delta\Omega \tag{4.4}$$

where N_0 is the total number of beam particles and n_t the areal number density of target nuclei. Through this equation we can relate the efficiency corrected number of counts to the differential cross section. The 16 rings in the FCD can be considered as 16 elements of solid angle $\Delta\Omega_i$. For each ring i with a central angle θ_i, the cross section is given by

$$\frac{d\sigma}{d\Omega}(\theta_i) = \left(\frac{1}{N_0 n_t}\right) \frac{N_{D,i}}{\epsilon\ \Delta\Omega_i} \equiv \frac{y_i}{S} \tag{4.5}$$

$$\text{where} \quad y_i = \frac{N_{D,i}}{\epsilon \Delta\Omega_i} \tag{4.6}$$

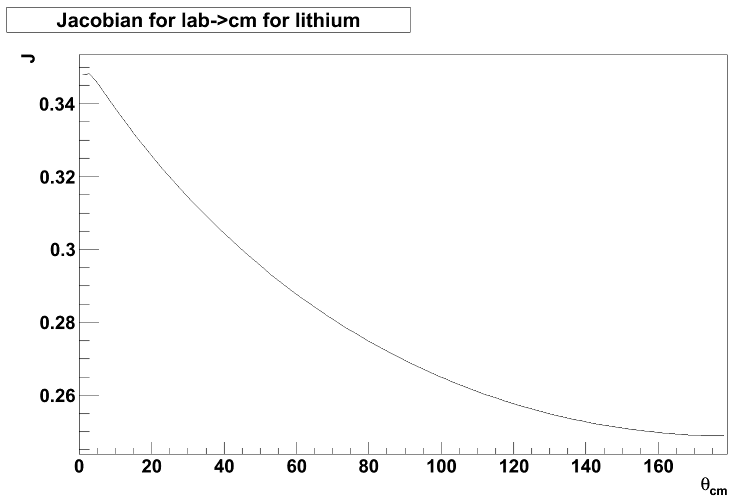

Figure 4.9: The *Jacobian* linking conserved distributions (with respect to solid angle) in the LAB frame with the CM frame for elastic scattering of ^{7}Li with ^{98}Rb. The cross-section in the LAB is transformed to the CM by simply multiplying with this function of the CM angle θ^*.

The quantity $S = N_0 n_t$ is the *scaling factor* from which the beam intensity can be extracted. The quantity y has been introduced for convenience, and will be referred to as the *unscaled cross-section.* The solid angle of each ring can be calculated exactly by assuming a pencil (point-like) beam. With the FCD so close to the target, this is quite an assumption. Its validity is discussed later on when the simulation is used for analysis.

In two body kinematics, the center of mass (CM) coordinate system is normally most convenient. Relativistic two body kinematics are comprehensively derived in ref. [34]. Differential cross-sections in different reference frames are related by the fact that the same number of particles must pass through the corresponding elements of solid angle in their respective reference frames. To transform the differential cross section from the lab to the CM frame it can be shown that [34]

$$\frac{d\sigma^*}{d\Omega^*} = J(\theta^*)\frac{d\sigma}{d\Omega} \tag{4.7}$$

$$\text{where} \quad J(\theta^*) = \frac{\left[\gamma^2(\cos(\theta^*)+r)^2+\sin^2(\theta^*)\right]^{3/2}}{\gamma|1+r\cos(\theta^*)|} \tag{4.8}$$

Here γ is the usual Lorentz factor and $r = \beta/B^*$ is the ratio of the velocity β of the CM frame with respect to the LAB frame and the velocity B^* of the particle in the CM frame. An example of this transformation *Jacobian* for lithium is shown in figure 4.9.

The differential cross section in the CM is then given by

$$\frac{d\sigma^*}{d\Omega^*}(\theta_i^*) = J(\theta_i^*)\left(\frac{y_i}{S}\right) = \frac{y_i^*}{S} \tag{4.9}$$

The Jacobian is evaluated at the CM angle corresponding to the mean lab angle of the ring, θ_i. The error δJ is estimated by evaluating J at the CM equivalents of the inner and outer ring angles.

The only unknown that remains is the number of beam particles N_0, which is contained in the scaling factor S. The unscaled cross-section y_i can be fitted to theoretical calculations to extract this value. Once a value for S has been extracted, it can be used for the other reaction channels. The error on the cross sections obtained in this way is given by:

$$\frac{\delta\left(\frac{d\sigma^*}{d\Omega^*}\right)}{\left(\frac{d\sigma^*}{d\Omega^*}\right)} = \sqrt{\left(\frac{\delta N_D}{N_D}\right)^2 + \left(\frac{\delta J(\theta^*)}{J(\theta^*)}\right)^2 + \left(\frac{\delta S}{S}\right)^2 + \left(\frac{\delta \epsilon}{\epsilon}\right)^2} \tag{4.10}$$

Though the elastic scattering of ^{7}Li is expected to be very close to Rutherford, small deviations are likely at larger angles are likely. The calculation of a theoretical cross-section is discussed in the section 4.7.

4.6 Simulation analysis

A simulation of the elastic scattering of ^{7}Li can be used to account for some of the steps taken in the analysis above. The simulation takes as input an angular distribution of the cross section, and completely simulates scattering and detection with the correct geometry, assuming a beam of 4 mm FWHM. A flat input cross section of $\frac{d\sigma}{d\Omega}(\theta^*) = 1$ mb/sr is most convenient for this method of analysis. From the simulation, the number of elastically scattered ^{7}Liparticles detected in each ring, $N_{D,i}$, is obtained. Rearranging equation 4.6 for $N_{D,i}$ and including the Jacobian factor to transform to CM yields

$$N_{D,i} = \frac{1}{S}\left(\frac{\epsilon \Delta\Omega_i}{J(\theta_i^*)}\right)\frac{d\sigma^*}{d\Omega^*}(\theta_i^*) \tag{4.11}$$

The quantities in brackets must be the same for both the simulated elastic scattering (will be denoted with primes) and the measured elastic scattering. The ratio of the number of counts therefore yields the differential cross section immediately:

$$\begin{aligned} \frac{N_{D,i}}{N'_{D,i}} &= \frac{S'}{S}\frac{\frac{d\sigma^*}{d\Omega^*}(\theta_i^*)}{\frac{d\sigma^*}{d\Omega^*}'(\theta_i^*)} && (4.12)\\ \therefore\ \frac{d\sigma^*}{d\Omega^*}(\theta_i^*) &= \frac{S'}{S}\frac{N_{D,i}}{N'_{D,i}} \times (1\ \text{mb/sr}) && (4.13)\\ \text{and}\ \ y_i^* &= \frac{S' N_{D,i}}{N'_{D,i}} \times (1\ \text{mb/sr}) && (4.14) \end{aligned}$$

The simulation scaling factor S' is determined by the total number of simulated scattering events. The unscaled cross-sections emerge surprisingly quickly from the simulation data and bypasses solid angle and efficiency considerations. The Jacobian factor only cancels when comparing elastic scattering with elastic scattering. It will still need to be calculated for reaction channels where mass is transferred.

This method is a good test of the steps taken in the previous section. Combining equations 4.14 and 4.6 the ratio of the unscaled cross sections obtained by calculation and simulation is given by

$$R_i = \frac{y^*_{i,calc}}{y^*_{i,sim}} = \frac{S' J_i}{N'_{D,i}\epsilon\Delta\Omega_i} \tag{4.15}$$

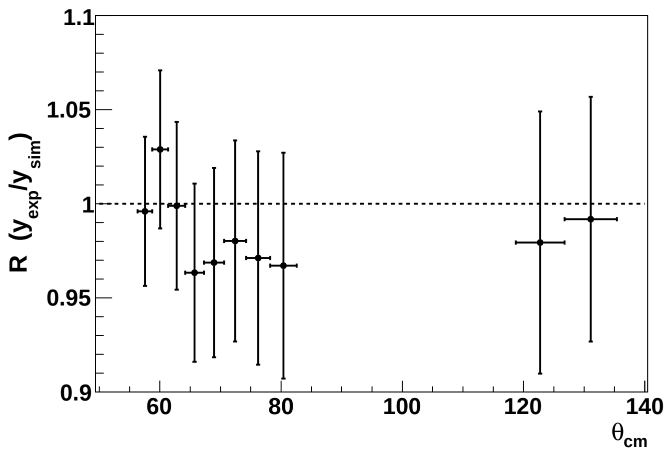

Figure 4.10: Ratio of unscaled cross-section of ^{7}Li obtained with calculations to that obtained using simulation data.

This ratio is plotted in figure 4.10. The errors are calculated by combining the relative errors $\delta J/J$ and $\delta\epsilon/\epsilon$ in equation 4.15 quadratically. The two methods agree closely, well within the error bars.

The equivalence of the two means of analysis shows that we have correctly accounted for the solid angle and geometry. The approximation of a pencil beam to calculate the solid angle is acceptable, and the Jacobian transformation to the CM frame is consistent.

Another use of the full simulation is to check how sensitive we are to the shape of an angular distribution. A fictional angular distribution with smooth oscillations in the range of our detector was used as input for the simulation. Analysis of these simulation results with both the simulation and calculation methods were successful in recovering the input cross-section. The broad range of angles integrated in each ring do not wash-out the shape of the angular distributions.

4.7 Fitting the elastic cross-section

To scale the elastic scattering cross-section calculations were made in the framework of an optical model using the FRESCO [22] code to determine the theoretical $\frac{d\sigma}{d\Omega}$. Such a calculation requires input parameters to define the nuclear part of the scattering potential. This input depends greatly on the amount of experimental work already performed on the nucleus in question. Global optical model potentials are constructed by simultaneously fitting the data from several experiments across a range of nuclei, including energy, mass and other dependencies. These potentials are particularly useful for poorly known nuclei, as is the case with ^{98}Rb. Such a compilation was performed by Cook [35] in 1982 for ^{7}Li in the mass and energy ranges A =24–208 and $E(^7\text{Li})$=28–88 MeV. Parameterized expressions for the optical model potential parameters were obtained.

Were the current experiment performed in direct kinematics, the corresponding energy of ^{7}Li mid-target would be 17 MeV, which falls outside the range of the fitted data. A more appropriate global optical-model potential could not be found. However, the use of this potential in spite of the energy being outside the appropriate range is somewhat justified. Firstly, in the fitting by Cook [35] no improvement in the χ^2 was found when including an energy dependence. The parameters can be assumed to vary slowly down to the energy of the current experiment. Secondly, the energy of the current experiment is below the coulomb barrier. The scattering should be Rutherford-like, with the coulomb potential playing a greater role than the nuclear potential. In a similar experiment of ^{7}Li on ^{80}Sn oscillations due to the nuclear potential were not seen up to energies 40% over the coulomb barrier [36]. With only one potential available for this calculation, it is difficult to estimate an error on the calculation.

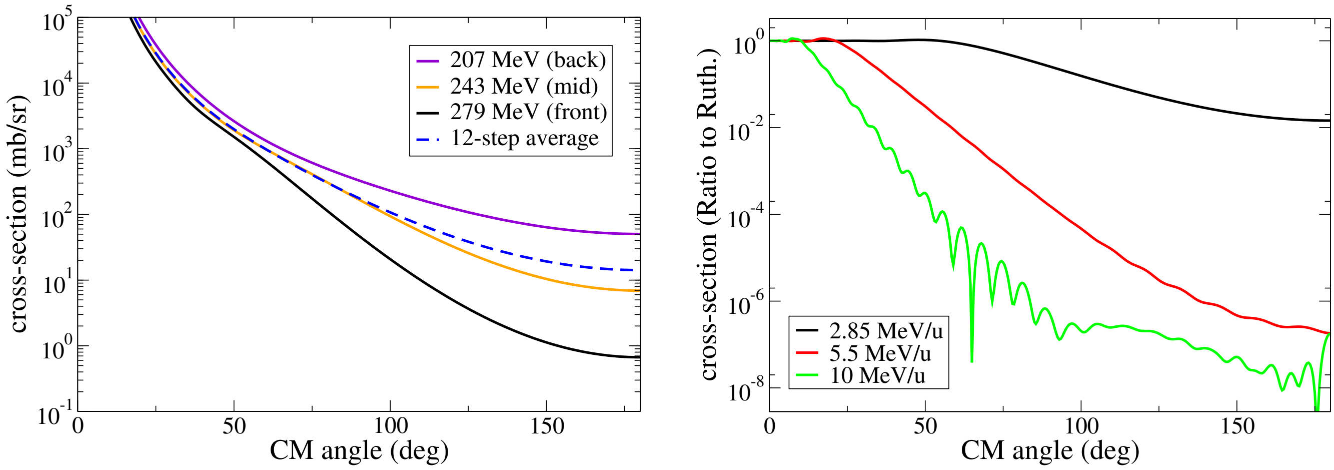

(a) (b)

Figure 4.11: Calculated cross-sections for ^{98}Rb+^{7}Li elastic scattering using global optical-model potential of Cook [35] at various energies. The blue-dashed curve is a 12-step numerical calculation of equation 4.16.

Figures 4.11 shows the calculated cross sections for ^{98}Rb on ^{7}Li for different energies. Indeed oscillations only seem to manifest well above the coulomb barrier for calculations with Cook's potential, as can be seen in figure 4.11b. Figure 4.11a shows calculations at energies corresponding to the front, middle and back of the target, which are the limits of our scattering problem.

Because of the thickness of the target, we must consider the effect of the broad range of effective beam energies on the differential scattering cross-section that we experimentally observe. Scattering occurs throughout the target with uniform intensity but depth dependent energy. The differential cross-section depends on the energy – for Rutherford-like elastic scattering as $1/E^2$. What we observe experimentally is an average scattering over the thickness of the target. The contribution to this average at higher energy in the front half of the target is less than the contribution at lower energy in the back of the target. Clearly a mid-target approximation, using the differential cross-section at the mid-target energy, breaks down for a thick target. The differential cross-section can be better described by a weighted average over the entire target thickness;

$$\left\langle \frac{d\sigma}{d\Omega} \right\rangle = \frac{1}{t} \int_{\text{target}} \frac{d\sigma}{d\Omega}(E(z))dz \tag{4.16}$$

The *average* cross-section was computed by numerically calculating the above integral. The result is shown in figure 4.11a, where the small difference with the mid-target approximation (243 MeV) can be noticed.

	Effective Variance			*Simple* χ^2		
E (MeV)	**S**	**% err.**	χ^2	**S**	**% err.**	χ^2
207	128 ± 6	5 %	10	115 ± 3	3 %	31
243	239 ± 11	5 %	48	220 ± 7	3 %	169
279	1158 ± 114	10 %	272	399 ± 15	4 %	527
avg	221 ± 10	5 %	13	230 ± 7	3 %	48

Table 4.1: Fitting results for the scaling factor S.

The experimental data was fitted to this averaged differential cross-section as well as the calculated differential cross-sections for energies corresponding to the front (279 MeV), middle (243 MeV) and rear (207 MeV) of the target for comparison. Two fitting procedures were used to fit the curves to the data. The first is a simple χ^2 minimization procedure that only considers the error on the ordinate Y

$$\chi^2 = \sum \left[\frac{Y - f(X)}{\delta Y}\right]^2 \tag{4.17}$$

where X is the coordinate. The second *effective variance method* assumes an uncorrelated error in Y due to the errors in X. The χ^2 is calculated with

$$\chi^2 = \sum \frac{(Y - f(X))^2}{\delta Y^2 + (f'(X)\delta X)^2} \tag{4.18}$$

The results of the two fitting procedures are given in table 4.1.

The meaning of an error bar in the X-axis is often scrutinized. For the current data, each data point is the result of an *integral* of the scattered particles in a finite solid angle. The impression that the data point could be anywhere along the horizontal error bar is not correct. The horizontal error bars are better interpreted as a bin width. The integrated average over these bins is plotted at the center of the bin. Nonetheless, it is necessary to systematically include the effect of the large range of angles integrated in each ring in order to obtain a more reasonable error on S. To this end the effective variance method of eq. 4.18 offers a simple solution.

The averaged curve reproduces the experimental data far better than the mid-target approximation is reflected in the values of χ^2 (table 4.1). Surprisingly, the rear target curve gives the lowest χ^2 value. The averaged curve however represents the physical situation more accurately than any single energy approximation. Therefore the effective variance fit to the averaged differential cross-section is accepted, giving a scaling factor of

$$S = 221 \pm 10\,\mathrm{mb}^{-1} \tag{4.19}$$

The elastic cross-section with this scaling is shown in figure 4.12. This of course also shows the effective variance fitting of the data points to the averaged cross-section. The calculated differential cross-sections for the front and rear target energies are included in the figure to emphasize that the differential cross-section we observe is an average over our target thickness.

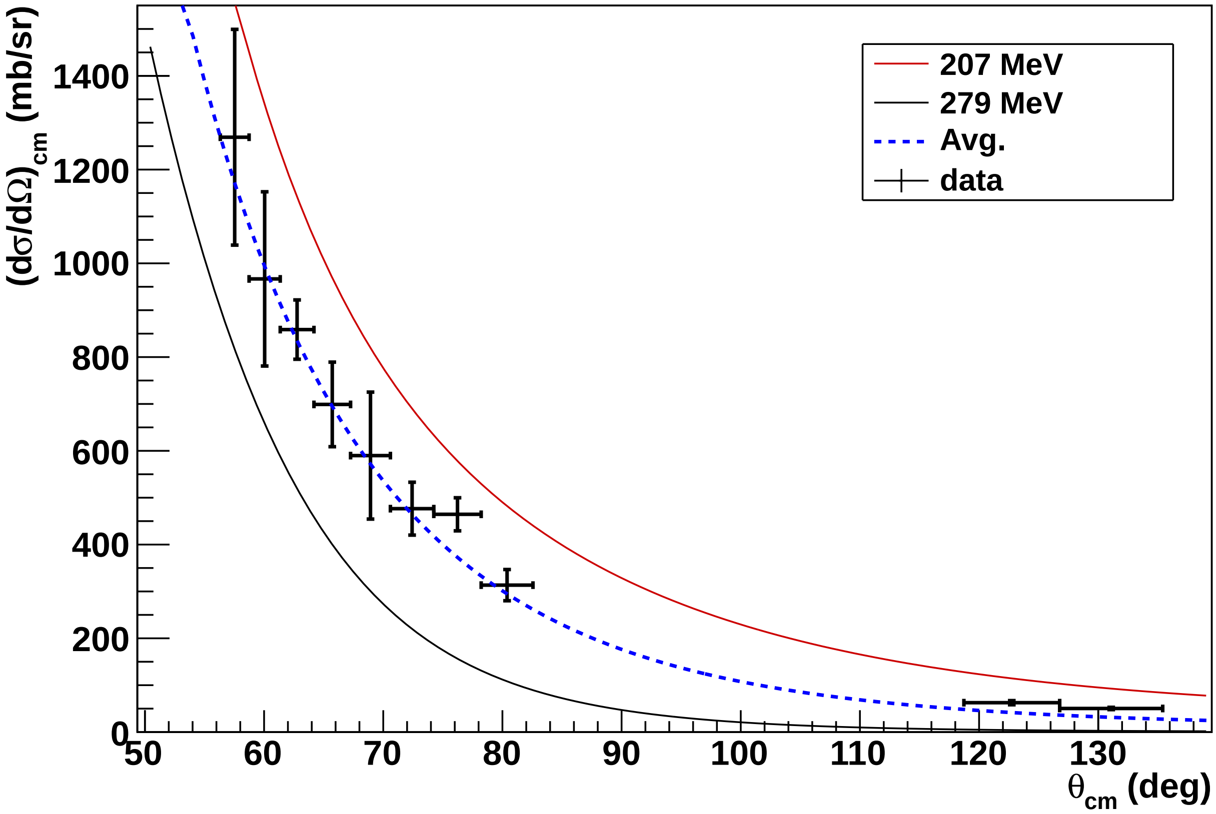

Figure 4.12: Differential cross-section for elastic scattering of ^{7}Li, fitted to the averaged cross-section (blue dashed line). The calculated cross-sections at the front (black curve) and rear (red curve) of the target are also shown.

From the scaling factor an average beam intensity can be extracted. The total beam time of the experiment is estimated at $T = 81 \pm 3$ hrs, taking into account interruptions in the beam and runs where the beam intensity was significantly lower. The target thickness is estimated at $n_t = 1.5 \pm 0.1$ mgcm^{-2}. The average beam intensity in particles per second is then:

$$\begin{aligned} I = \frac{S}{n_t T} &= 2.16 \times 10^4 \,\text{pps} \\ \delta I_{\text{systematic}} &= 0.12 \times 10^4 \,\text{pps} \\ \delta I_{\text{fitting}} &= 0.1 \times 10^4 \,\text{pps} \end{aligned} \tag{4.20}$$

The systematic error $\delta I_{\text{systematic}}$ includes uncertainty on the time T and target thickness n_t. The fitting error depends on statistics, and the theoretical calculation used to fit. The error on the theoretical calculation cannot be easily estimated. Combining the two errors quadratically, gives an uncertainty of the beam intensity of 7%.

Chapter 5

Results and Discussion

5.1 Angular distributions

5.1.1 Elastic Scattering

The angular distribution for the elastic scattering of ^{98}Rb on ^{7}Li is shown in figure 4.12. The leftmost point corresponds to the outer ring at maximum lab angle, and the rightmost to the inner ring. The curve to which the data was scaled – the energy averaged calculated cross-section – is plotted along with calculated cross-sections using beam energies at the front and rear of the target. The curves corresponding to the front and the rear of the target are shown to emphasize the fact that the cross-section we observe is a weighted average over the target thickness of the cross-sections between these curves (see equation 4.16). This average was approximated numerically, and was found to fit the data well.

The gap in the data due to insufficient full-scale range on the ΔE detectors separates points where N_D was determined by fitting (low θ_{cm}) and ΔE-E particle identification (high θ_{cm}). In both cases the error on N_D was the greatest source of uncertainty, due to fitting and low statistics respectively.

The single neutron transfer channels cannot be separated from the elastic ^{7}Li, and may well be contributing to the ^{7}Li counts. These channels are expected to be of the order of a few millibarn, negligible compared to the elastic scattering which is of the order of hundreds of millibarn. The fact that a calculation of only elastic scattering fits the data within the error bars confirms that this is indeed the case.

The differential cross-section for elastic scattering of protons, which were present as a contaminant on the target, is shown in figure 5.1. The energy in the CM frame is well below the Coulomb barrier, and so the scattering is expected to be Rutherford. The data was fitted to the Rutherford cross-section at the mid-target energy. The fit is poor, with $\chi^2 = 66$. As these contaminant protons are not of interest in this work, the reassurance of the elastic scattering analysis method that we observe here is sufficient and so it was not considered worthwhile to improve the fit. However, a rough estimate of the number of protons in the target can still be extracted from the obtained proton scaling factor. We find for the number of protons a fraction of $2.9 \pm 0.2\,\%$ of the number of ^{7}Li atoms, which is consistent with suface contamination of the target by water deposition.

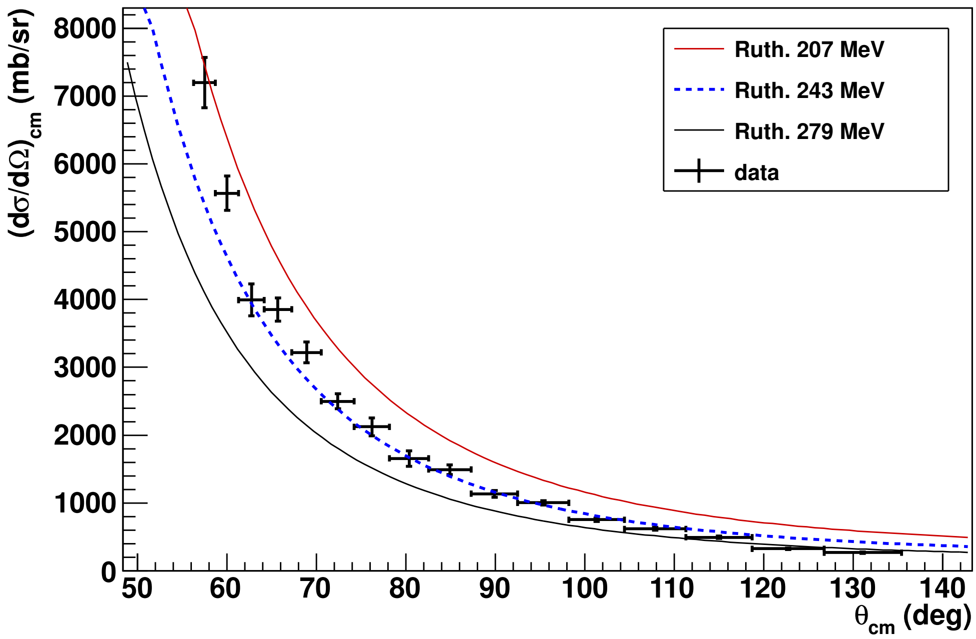

Figure 5.1: Differential cross-section for elastic scattering of protons. Fitted to the Rutherford cross section at the mid-target energy (blue dashed curve. The Rutherford cross-sections at the front (black curve) and rear (red curve) of the target are also shown

5.1.2 Cluster Transfer Reactions

The α- and triton-transfer channels are the cluster-transfer reactions of interest with a ^{7}Li target. They were seen to be the strongest (as can be seen in figure 4.2), and were easily identified where they punched through. The analysis of the elastic scattering channel provided a scaling factor for the differential cross-sections of the α-particle and triton channels, shown in figures 5.2.

The differential cross-section for the (^{7}Li,^{6}He) channel was also extracted, because it was well-separated in the ΔE-E matrix and unexpectedly strong. Though it is not a reaction channel of particular interest, it serves an extra test of the punch-through limits of the experimental setup because of the large mass of the nucleus.

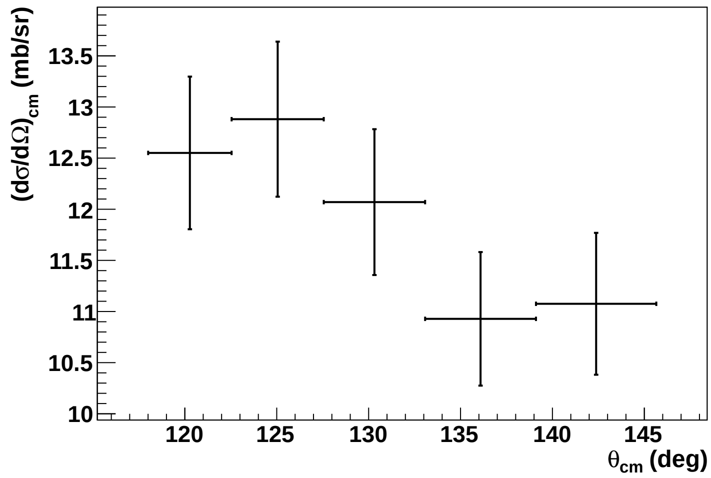

(a) α-particles (associated with triton-transfer)

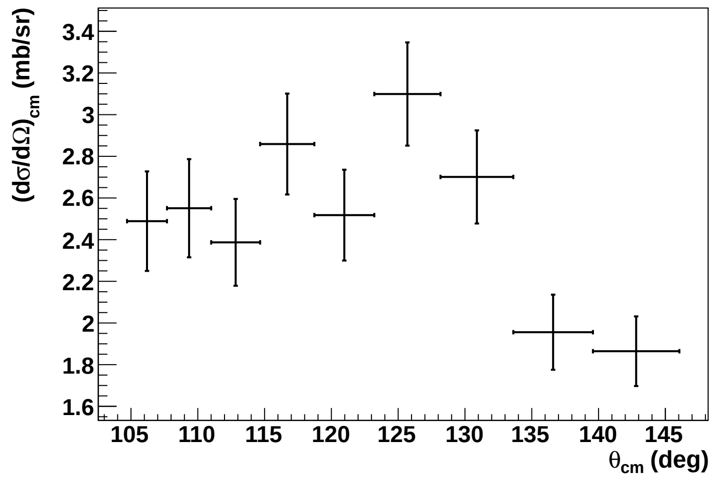

(b) Tritons (associated with α-transfer)

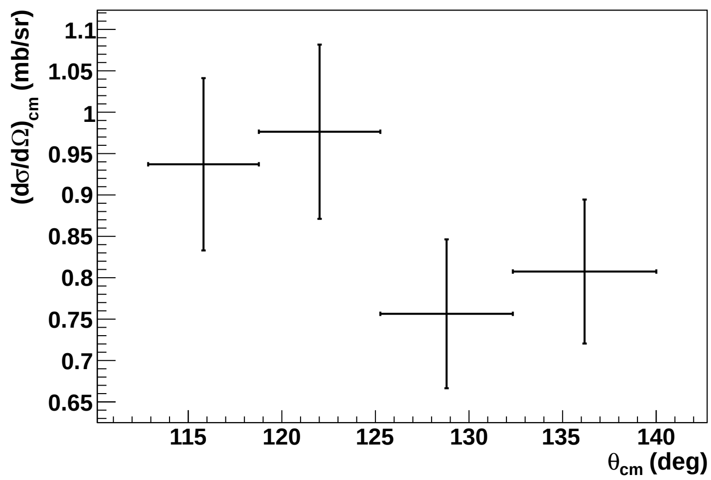

(c) ^{6}He (associated with proton-transfer)

Figure 5.2: Differential cross-sections for cluster-transfer channels. Note that the differential cross-sections for the α-particle and triton channels contain events from breakup.

5.2 Integrated cross-sections

To be able to compare the cross sections for the different channels it is useful to integrate them over common ranges of angles. In the lab frame, the opening angles of the rings are the same for each particle and integration over a common range of solid angles is straightforward.

In the CM frame, the common geometry in the lab frame for the different particles is affected by the transformation. Fortunately, between α-particles and tritons the change in center of mass angle is negligible. This is not the case for ^{7}Li. The results for both reference frames are given in table 5.1 for the integration of the 5 innermost rings where both α-particles and tritons punch through. If integration is done in the discrete steps of the ring geometry in either reference frame no numerical error is introduced.

		θ_a [°]	θ_b[°]	σ_{ab} [mb]
α	CM	118	146	26.6 ± 0.7
t	CM	119	146	5.3 ± 0.2
^{7}Li	CM	98.5	135.5	213 ± 1
^{7}Li	CM*	118.0	145.5	73.4 ± 0.8

Table 5.1: Integrated cross-sections for common element of solid angle. For lithium, the average calculated curve was integrated numerically. All entries except for the (*) ^{7}Li correspond to the inner 5 rings in the lab frame ($22° - 40.8°$).

For ^{7}Li the (averaged) theoretical curve is integrated numerically. The starred result is the integral over the common CM range shared by the α-particles and tritons. These cross-sections are directly comparable with eachother. The ratio of the α-particles to the tritons is shown for common rings in figure 5.3. Integrated over the (approximately) common CM range of $118° - 146°$ the ratio is found to be

$$\frac{\sigma_\alpha}{\sigma_t} = 5.0 \pm 0.2 \tag{5.1}$$

The measured α-triton ratio is comparable to the result of 4 obtained in an experiment of ^{7}Li+^{184}W at 55 MeV [9].

The total cross-sections for all the ΔE-E identified particles are given in table 5.2. The unexpectedly large measured cross-sections for the α-particle and triton channels are a very encouraging result. With the low beam intensity of 2.16×10^4 pps, the statistics for the much smaller cross-sections predicted before the experiment may well have been to low.

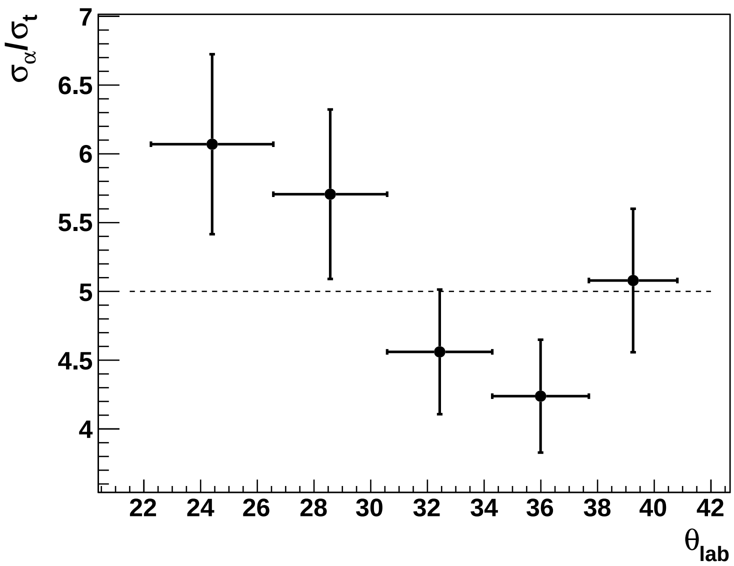

Figure 5.3: Ratio of α-particle over triton cross-sections. Plotted as a function of lab angle where the angular ranges of each ring are equal, though the ranges in the CM coincide very closely for each ring. The ratio of the integrated cross sections is plotted as the dashed line.

	ΔE **punch-through**	σ_{TOT}
t	inner 9 rings	9.0 ± 0.3
α	inner 5 rings	26.6 ± 0.7
^{6}He	inner 4 rings	2.1 ± 0.1
^{7}Li	inner 2 rings	82 ± 4

Table 5.2: Total integrated cross-sections σ_{TOT} for particles that punch through the ΔE detector.

5.3 Gamma spectroscopy

The combination of information obtained from particle detection and gamma-spectroscopy is possibly the most significant advantage of a cluster-transfer experiment. Up until now, the focus has been on the analysis of the particles, which was the focus of the work for this thesis. The gamma-rays were analyzed by S. Bottoni[1] in parallel. Some preliminary results are presented here for completeness.

The strength of the current experiment lies in the particle-gamma coincidence. By detecting particles, we are able to gate on a particular cluster-transfer channel. Following the transfer of a cluster, the residual nucleus is left in an excited state, and will proceed to evapourate neutrons if the excitation energy exceeds the neutron separation energy. After the release of neutrons to reduce the excitation energy of the nucleus to below the neutron separation energy, the nucleus is still in an excited state, and will proceed to release the remaining energy through a cascade of γ-rays. The above process is instantaneous on

[1] Joint PhD student of KULeuven and University of Milan.

the timescale of the detection setup, and so γ-rays can be detected in coincidence with the particle that identifies the initial transfer channel. This dramatically reduces the background of the γ-spectra. Furthermore, the energy and mass of the light particle can be used to do accurate Doppler correction of the γ-energy, improving the resolution of the γ.

Figure 5.4 shows the nuclei for which known gamma-rays were observed in coincidence with the cluster-transfer particles. Though the ^{98}Sr component in the beam was irrelevant for the determination of the cluster-transfer cross-sections, it cannot be ignored here as we clearly see the products resulting from cluster-transfer on ^{98}Sr followed by neutron evaporation. For both beam nuclei at least two neutrons were evaporated after cluster transfer. This is consistent with the very high excitation energy of the residual nucleus (see table 3.3).

After neutron evaporation the residual nucleus is still at a very high excitation energy. The continuous energy spectrum of neutron evaporation together with the high density of states at such high excitation energy ensure that very many different excited states are populated. The different excited states initially cascade through different paths in the dense energy spectrum, emitting low energy γ-rays en route. The intensities of the γ-rays are too low to be observed until the density of states has decreased enough for these paths to converge. The highest spin that was observed in this experiment was $13/2^+$, identified by a transition from the 706.1 keV $13/2^+$ state in ^{99}Y. Though we likely populate the nuclei at higher excitation than this after the neutron evaporation, the γ-rays from which we could conclude this are by the above considerations not intense enough.

The γ-rays can be used to estimate the contribution of breakup to the α-particles and tritons by assuming very crudely that all excited states of the residual nuclei produced in transfer pass through the first excited state en route to the ground state, emitting the corresponding γ-ray. The sum of the particle-γ coincidences of the γ-rays from this transition over all the residual nuclei populated by the transfer channel of the particle can be compared to the particle-γ anti-coincidences to obtain an upper limit

$$\frac{Y_{\text{breakup}}}{Y_{\text{transfer}}} \leq \frac{N(\text{particles without } \gamma)}{\sum_i N(\text{particles with } \gamma_i)} \tag{5.2}$$

where the sum over i indicates a sum over all the residual nuclei from the cluster transfer channel, and γ_i is the corresponding γ-ray of the transition from the first excited to the ground state. Considering both the α-particles and the tritons (separately) the ratio is found to be $19 \pm 7\,\%$.

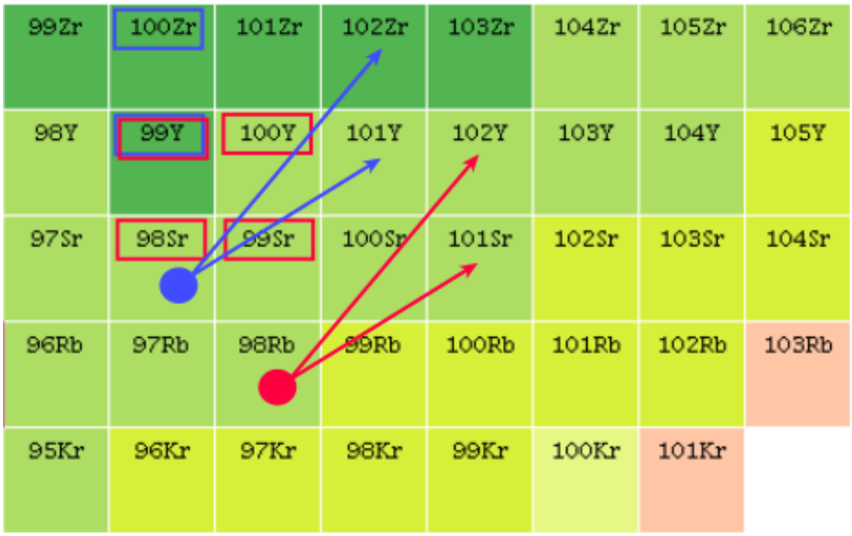

Figure 5.4: Nuclei for which γ-rays were observed. Products of cluster-transfer following neutron evaporation on ^{98}Rb are circled in red, and ^{98}Sr in blue. The nuclei produced in α- and triton transfer are indicated with arrows of corresponding colours.

5.4 Comparison with theory

The measured angular distributions for the detection of α-particles and tritons can now be compared with theoretical calculations. Though the measured cross-sections certainly include breakup, we saw in the analysis of the γ-rays that this contributes a fraction of approximately 1/5. Theoretical predictions for cluster-transfer cross-sections are currently far from this accuracy – we are still looking for reliable order of magnitude agreement with calculations. The absolute cross-sections may indeed be very difficult to reproduce, but for the ^{7}Li case we have the two strong α- and triton-transfer channels, the ratio of which should be reproduced by any useful model.

5.4.1 Wilczyński Sum-rule model for incomplete fusion

The Wilczynski Sum-rule model is only capable of calculating the total cross-sections for the different reaction channels, in the regime of incomplete fusion. Though what we measure are differential cross-sections, the very inverse kinematics can focus the cross-sections into a very broad forward cone in the lab frame which could be completely covered, so if this model is able to reproduce the correct orders of magnitude it could be useful for future predictions. Here we assume that the differential cross-sections for each incomplete fusion channel have a similar angular distribution, such that the total cross-sections for each particle should be in approximate proportion to the differential cross-sections.

A code was developed to perform calculations in the Sum-rule model, following the formulation by Wilczński et. al. in ref. [16]. The first step in making calculations for the ^{7}Li+^{98}Rb system would be of course to successfully reproduce the results of Wilczynski et al. [16]. Trying to implement the model however revealed some vaguenesses in its formulation, which have as much freedom for the resulting cross-sections as the three free parameters do. One must make a choice as to exactly which channels are included in the Sum-rule. In ref. [16] the incomplete fusion channels where mass is transferred from

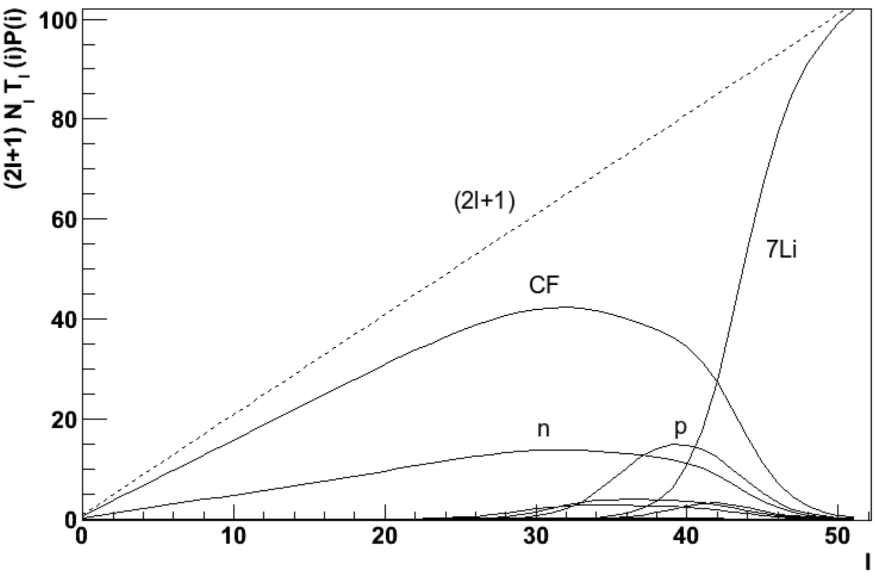

Figure 5.5: Contributions of the different incomplete fusion reaction channels calculated in the Wilczyński sum-rule model. The cross-section for each process is proportional to the integral of each curve. Curves are labeled by the outgoing particle.

heavy to light at higher l_{crit} were included in the calculation. How l_{max}, the maximum angular momentum for which any incomplete fusion process can occur, would be defined in this case is not clear. Futhermore, a process of mass transfer in both directions (eg. proton from light to heavy and a neutron from heavy to light) was also included. In other works [9, 17], only incomplete fusion where mass is transferred from light to heavy were included. Nonetheless, the implementation done in this work managed to reproduce the probability distributions in l-space for all but one of the reaction channels treated in the ^{14}N+^{159}Tb system of Wilczynski et al. [16].

Application of the model to ^{7}Li incomplete fusion reactions was performed by Clark et al. [9] for the ^{7}Li+^{184}W system in an experiment where *differential* cross-sections were measured for different beam energies using an annular detector. Slightly different parameters were used to provide a very good fit of the α-triton cross-section ratio for a beam energy of 55 MeV ^{7}Li. Too few details of the calculation were provided for this number to be reproduced, so the success of the model in this case should be regarded with care.

In light of the above, and because there is no obvious reason to change the original parameters of Wilczynski et al. [16], the original parameters were used unaltered for the calculation of our ^{7}Li+^{98}Rb system. l_{max} was taken as the value for which the unnormalized probability of the highest l_{lim} process dropped below 1% of its maximum. To ensure the convergence of incomplete fusion cross-sections in this definition of l_{max}, the non-fusion (^{7}Li,^{7}Li$^{(*)}$) channel had to be included. Elastic scattering would have an arbitrarily large limiting angular momentum l_{lim}, giving the channel a unity contribution to the Sum-Rule which dominates the sum for $l > l_{\text{max}}$.

A plot of the normalized probabilities (including the factor $(2l+1)$) for each reaction channel is shown in figure 5.5. The cross-section for each channel is proportional to the integral of the curve. The result is not very promising. The magnitudes of the total cross-sections for each included channel are given in table 5.3. Neither the cross-sections nor the relative strengths of the various channels agree with what was experimentally

Fusion	**Detection**	σ_i **(mb)**
n	^{6}Li	144
p	^{6}He	864
d	^{5}He	317
t	^{4}He	265
^{4}He	t	36.5
^{5}He	d	25.1
^{6}He	p	38.4
^{6}Li	n	2348
CF	/	7291

$$\frac{\sigma(\text{t-transfer})}{\sigma(\alpha\text{–transfer})} = 7.3$$

Table 5.3: Total cross-sections for incomplete fusion calculated with the Sum-rule model. All channels included in the calculation (except elastic) are shown.

observed.

The result depends quite strongly on the parameters, and can be adjusted to reproduce the α-triton ratio, but never produces any overall correspondence with the intensities of the different channels that we observed. This could be due to either inherent limitations of this semi-classical model, or because of the comparably low energy at which we are attempting to describe our system as incomplete fusion. The experiments where this model has been successful have all been performed well above the Coulomb barrier. So to conclude, one could say that the lack of detailed agreement with experiment from such a simple model is not surprising. On the same note then, we should be very sceptical of a single detailed agreement such as the α-triton ratio in amongst so many adjustable parameters.

5.4.2 Cluster-transfer

The model of Cluster-transfer and how calculations can be performed under DWBA is presented in section 2. Such calculations for the case of ^{98}Rb on ^{7}Li were performed by S. Bottoni for the cases of α- and triton-transfer.

Calculations assuming transfer to bound states of the composite nucleus are shown in figure 5.6. Such calculations were performed before the experiment, to estimate the expected magnitude of the cross sections for the cluster-transfer channels. The grey data points are the results of section 5.1.2 – the differential cross-sections for the α-particle and triton channels. These points are rescaled to the theoretical curves for comparison. α-particles are underestimated by two orders of magnitude, and tritons by four. At the very least, the disagreement of the ratio of detected α-particles to tritons by two orders of magnitude indicates that the model is failing terribly.

We have seen from the kinematics (see $E(\theta)$ plots of figure 4.3) that the cluster transfer is taking place to very high excitation energies in the residual nuclei. This is explained in the framework of the optimum Q-value in section 3.3 using the model of Brink [30]. The excitation energies are so high that they exceed the binding energies of the α-particle and triton in the ^{98}Rb and ^{98}Sr nuclei. The binding energies are shown in table 5.4. The transfer is taking place to unbound continuum states.

	Residual nucleus	**Binding energy**	**Observed E_x**
t-transfer	^{101}Sr = ^{98}Rb + t	16.5	20
	^{101}Y = ^{98}Sr + t	13.6	20
α-transfer	^{102}Y = ^{98}Rb + ^{4}He	10.4	18
	^{102}Zr = ^{98}Sr + ^{4}He	7.58	18

Table 5.4: Comparison of binding energies of the transferred cluster and observed excitation energies in units of MeV. The observed excitation energies are from $E(\theta)$ kinematics in figures 4.3 (^{98}Rb and ^{98}Sr are not distinguished).

To handle such a process in a DWBA coupled channels approach, one must proceed to construct states within the continuum using the Continuum Discretized Coupled Channels (CDCC) method. Such calculations for cluster-transfer are still being developed. A preliminary result, in first order DWBA, is given in figure 5.7. Here a *common* rescaling is applied to the experimental points.

The absolute cross-sections are not exactly reproduced but the calculation is at the correct order of magnitude, which is an important first step at such a young stage of Cluster-transfer theory. More importantly, the ratio between the two transfer channels is of satisfactory agreement with the data. The resulting shapes are not reproduced, but at these large CM angles where the behaviour is very sensitive to the nuclear potentials this should not too surprising.

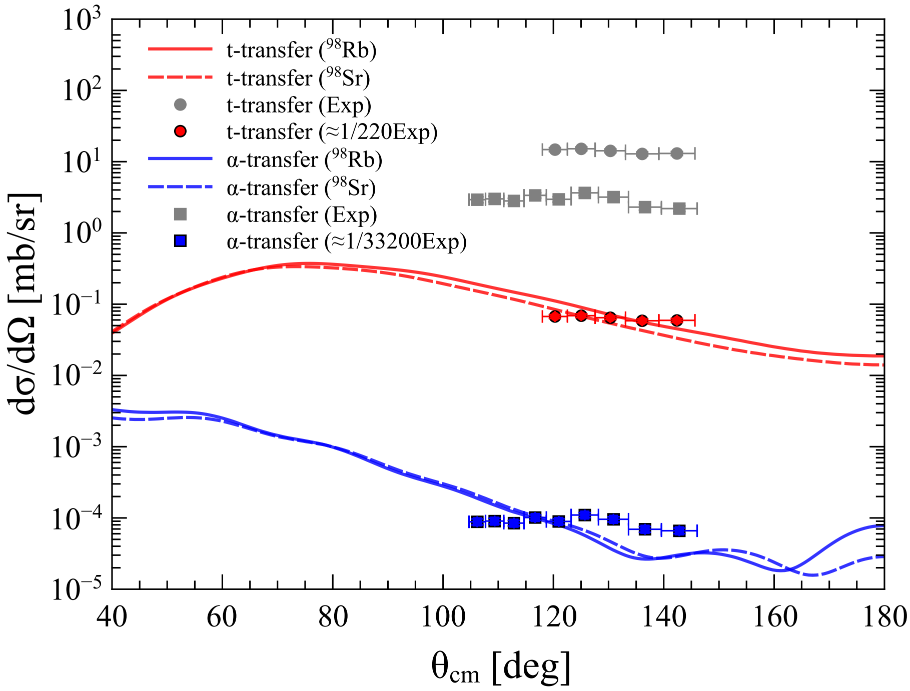

Figure 5.6: DWBA Cluster-transfer calculation for transfer to bound states. *Courtesy of S. Bottoni.*

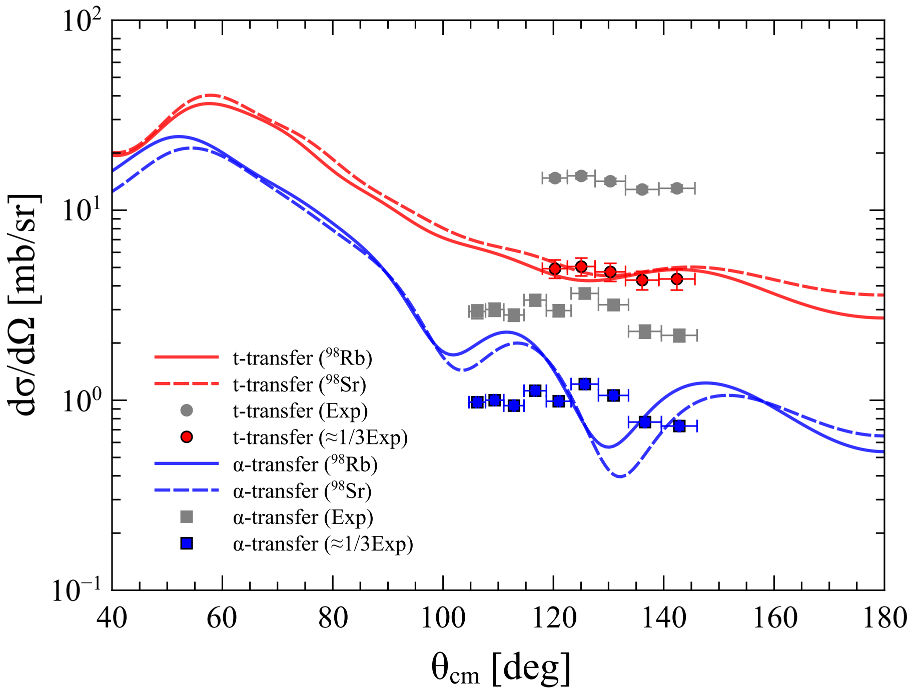

Figure 5.7: DWBA Cluster-transfer calculation for transfer to discretized continuum states (CDCC). *Courtesy of S. Bottoni.*

Chapter 6

Outlook

This experiment serves as a starting block for the study of cluster-transfer reactions at ISOLDE. By acquiring practical experience and measuring the cross-sections of the light particles associated with the transfer channels, we are able to make estimates of what is possible in the future. The experiment also provides useful testing grounds for the development of theoretical descriptions of the transfer process. This chapter presents both the theoretical and experimental insights gained thusfar as a conclusion to the thesis.

6.1 Towards a better theoretical description

In the previous chapter the data was compared with two different models, corresponding to two different descriptions of the massive transfer of a cluster. Whatever name is given to this process, one must not lose sight of the fact that we are describing the same particles in the entrance and exit channels. We send the projectile onto the target, and detect the outcoming particles, observing that some mass has been exchanged in the process. The nature of this mechanism could be compound, direct or a mixture of both. The names incomplete fusion and cluster transfer refer to different descriptions of the process, in a compound or direct formalism. One then asks the question: "which is correct?" and to this there is no simple answer.

The incomplete fusion description in the Sum-rule model of Wilczynski et al. [16] was not successful in reproducing our experimental results, under the crude assumption that the total cross-sections are directly comparable to the partial cross-sections for the angular range covered in the experiment (table 5.1). Previous successes of this model appear to be to confined heavier cluster nuclei at energies well above the Coulomb barrier [18, 17, 14]. Though some agreement was observed for the case of ^{7}Li in the work of Clark et al. [9], this experiment was performed well above the Coulomb barrier. A more careful treatment of the free parameters could help to identify where and why the calculation is failing. Such a simple model has the advantage of being easily extended. For example a more detailed "Modified Sum-rule model" has been recently proposed by Bhujang et al. [19] where the inclusion of an energy dependent term in the critical angular momentum has been shown to improve the results significantly.

In the direct reaction picture, the Cluster-transfer description was much more successful. DWBA Coupled Channels calculations were performed to calculate the differential cross-sections for the α- and triton-transfer processes. We observed transfer to very high excitation in the residual nucleus, well above the binding energy, which made necessary the CDCC (Continuum Discretized Coupled Channels) formalism, to treat the transfer to unbound states. The preliminary results were able to reproduce well the ratio of α-particles to tritons, which is an exciting first step in the theory.

Of course we cannot completely discard the fusion nature of the process simply due to the success of the CDCC calculation and the failure of the very simplistic Sum-rule model. There exist many other models which have the potential to describe our system. Consider for example the work of Shrivastava et al. [37], where the reaction mechanism is treated as a two-step "breakup-fusion" process to successfully describe the massive transfer reactions of the ^{7}Li + ^{198}Pb system. Here, a classical dynamical trajectory model [38] provides a stochastic treatment of the breakup process. Again, this description was applied above the Coulomb barrier.

The above example also shows how useful classical descriptions in the problem of cluster-transfer appear to be. At such high, continuous excitation energies and large angular momenta this feels somewhat reasonable. Indeed in our analysis, very simple semi-classical calculations proved their worth with the calculations performed in the optimum Q-value formalism of Brink [30] which predicted quite well the excitation energies that we observed.

Much work remains to be done to find reliable descriptions of the massive transfer with the weakly bound ^{7}Li nucleus over a wide range of energies above and below the Coulomb barrier. What we can conclude from the preliminary theoretical cluster-transfer calculations for our system very close to the Coulomb barrier is that the reaction mechanisms for the α- and triton transfer channels are very well described by a direct cluster-transfer to continuum unbound states.

6.2 Experimental insights

The analysis of the particles detected in the FCD annular detector formed the largest part of the work for this master thesis. When theoretical predictions of cross-sections for an experiment are unreliable, we need to be confident with the experimental setup. In the region of exotic nuclei, low beam intensities and small cross-sections come with the territory, and so particle detection should be as comprehensive as possible. In light of the challenges faced in this experiment, some suggestions can be made for future experiments with a ^{7}Li target, and possibly T-REX.

Firstly, the measured cross-sections for α-particles and tritons are very encouraging, considerably higher than predicted by the calculations for transfer to bound states performed before the experiment. The average beam intensity was found in the analysis of elastic scattering to be low at 2.16×10^{4} pps. This was due to particular difficulties in producing ^{98}Rb and frequenct interruptions in beam. The beam composition was also quite mixed, containing ^{98}Rb and its isomer, as well as ^{98}Sr from β-decay. Needless to say, the beam was far from optimal. Because of the large cross-sections, we were still able to measure good statistics on the particles, which bodes well for heavier exotic beams where the similar problems are likely to occur.

For the study of the cluster-transfer mechanism itself, the target was perhaps too thick. The $1.5\,\mathrm{mg/cm^2}$ target caused significant energy loss of the ^{98}Rb nucleus, leading to a range of beam energies of 70 MeV over its thickness. The resultant broadening in the kinematic ($E(\theta)$) plots of figures 4.4 and 4.3 is translated to broadening of the excitation energy of the residual nucleus. With the measured cross-sections, taking a thinner target to improve resolution in excitation energy is possible. However, if cluster-transfer reactions are to be simply used as a tool to populate nuclei in the region of the target nucleus at high excitation for γ-spectroscopic study, this excitation energy is not of great importance. The increase in counts from a thicker target is then well worth the loss in resolution.

With regards to particle identification, the cluster-transfer particles from ^{7}Li are somewhat more difficult than conventional transfer ejectiles. α-particles and tritons are heavier than the protons and deuterons that are seen in conventional transfer reactions and so their energy loss is much larger. Particles not punching-through is therefore a significant problem.

The situation is worsened by the higher excitation energy of the residual nucleus in massive transfer. The effect of the excitation of the residual nucleus is to make less energy available for the kinetic energy of the outgoing particles. This can be visualized as a downscaling of the kinematic lines in figure 4.4 towards lower energies. The transfer particles in the exit channel therefore have very low energy. With the geometry of our annular detector – placed very close to the target – the effective thickness of the ΔE detector increases quickly towards the larger lab angles that we cover. At the same time the kinematic lines decrease in energy towards wider angles. Particles are therefore stopped in the outer rings of the annular detector, and cannot be ΔE-E identified. The combination of the above factors in this experiment meant that for α-particles, only the inner 5 rings of the FCD detector could be used. For ^{6}He only the four inner rings could be used.

Due to the success of the CDCC calculation in reproducing our data (figure 5.7), we can use it to estimate at which lab angles the cross-sections are maximum. Going forward, this is a very useful result as such calculations can be performed to guide our experimental setup to cover angles of maximum cross-section. For our system, the calculated differential cross-sections for both the α-particles and tritons predict an increase towards a broad maximum in the region of 90° in the lab ($\sim 60°$ in CM). The unfortunate reality is the fact that at these large lab angles the energy of the transfer ejectile is a minimum due to the kinematics, as can be seen in figure 4.4. This is the case for much heavier nuclei as well if we consider the same beam energy per nucleon. Experimentally, we cannot identify the particles in the region where we expect the maximum cross-section, regardless of the geometry of our detectors.

In light of the above obstacles for particle identification, we can consider how to improve the detector arrangement by minimizing the effective thickness of the ΔE silicon, which is what limits the punch-through. Thinner detectors are available[1], but are difficult to work with and come at the price of poor energy resolution. However, we saw in this work that the α-particles and tritons were well separated in the ΔE-E matrix (figure 4.2), and so we could afford the decrease in energy resolution.

A very simple improvement to angular resolution would be to simply move the annular detector backwards. Moving the detector 20 mm backwards would provide the same useable solid angle, but with the full 16-fold segmentation.

Including the forward barrel of TREX would cover the angles of larger cross-section, but would the particles punch-through the 140 μm Si? Considering the specific case of

[1] For example in the work of Shrivastava et al. [37] $25 - 30\,\mu$m ΔE detectors were used.

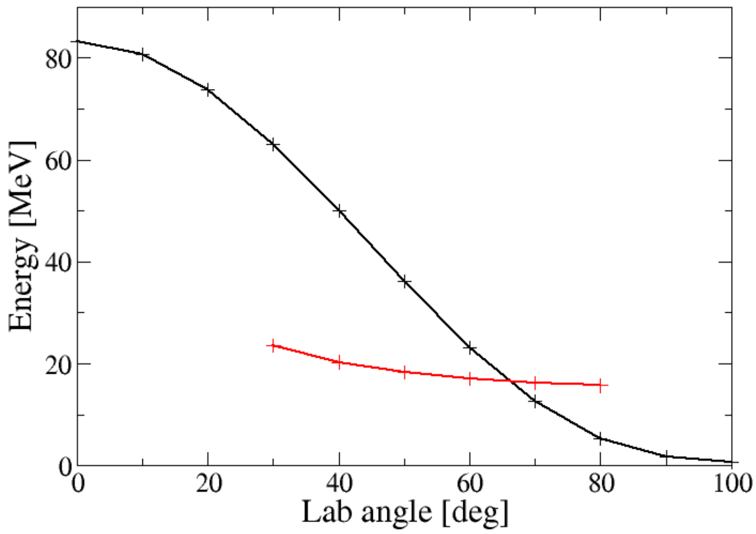

Figure 6.1: Kinematic line of the emitted α-particles from triton transfer from ^{7}Li on ^{132}Sn (black curve). The punch-through energy versus lab-angle of the TREX forward barrel is shown for the approximate range of angles it covers (red curve).

^{132}Sn on ^{7}Li at the HIE-ISOLDE beam energy of 5.5 MeV/u, producing the residual nucleus ^{135}Sb at an assumed excitation energy of 20 MeV, we see a similar kinematic situation as for the current experiment, with the energy of the α-particle dropping sharply by 90° (see figure 6.1). α-particles with energy below 16.0 MeV will be stopped in a 140 μm ΔE detector. The kinematic line drops below this energy at approximately 65°. Considering the effective thickness of the 140 μm ΔE of the barrel, the punch-through energy as a function of lab angle can be estimated[2]. The result is included in figure 6.1 for the approximate range of the barrel. These considerations do not include energy loss in the target, which could lower significantly the energies of the outgoing particles.

Clearly, the detection of the α-particles and tritons associated with cluster-transfer should be carefully considered. The shape of the kinematics do not change significantly for different (heavy) beam nuclei. The beam energy and the excitation energy for a given setup are what determine the range of angles for which we will be able to identify the particles. A reliable estimate of the excitation energy is crucial in planning a measurement.

6.3 Prospects for exotic nuclei

Cluster-transfer reactions with ^{7}Li have the ability to transfer more nucleons to the heavy nucleus than conventional transfer reactions. In the exploration of exotic nuclei, this reaction could offer us new pathways towards populating certain nuclei. In the ideal case, the transfer of a triton can take us to even more neutron rich nuclei.

However, we are at the mercy of neutron evapouration. Depending on the excitation

[2] Here we ignore the azimuthal dependence of the effective thickness due to the non-cylindrical box-like geometry of the barrel. The effective thickness t' is calculated by $t' = {}^{t}/_{\sin\theta}$

energy, neutron evapouration will take us back towards stability, away from neutron rich exotic nuclei. In this work we observed transfer to very high excitations of the residual nucleus and could explain this in terms of the semi-classical model of Brink [30]. Even with a low beam energy, just at the Coulomb barrier, the excitation energy was so high that we only observed gamma-rays corresponding to two and three neutron evapouration products of the residual nuclei, with the three neutron evaporation channel the strongest.

Because the high excitation is appears to be a characteristic of these cluster transfer reactions, the evaporation of several neutrons can be expected for other systems. In particular cases where the heavy beam nucleus is very tightly bound, such as the doubly magic ^{208}Pb and ^{132}Sn cases of interest, the Q-value and excitation energy may not be too high. The neutron evaporation would then be much less dramatic. Though these reactions do not appear to be very adept at reaching more neutron rich exotic nuclei, they still offer us a novel way to populate nuclei, which is definitely useful in exotic regions where some nuclei are particularly difficult to reach.

Perhaps the most important result of this work is that the cross-sections for the α- and triton-transfer reactions were found to be encouragingly large. These reactions are indeed feasible with the very low beam intensities charateristic of RIBs of exotic nuclei.

The particle-γ coincidence offered by the reaction mechanism were seen to be very useful in the analysis of the γ-spectra greatly reducing background and enabling good Doppler correction. Transitions from high spin states up to 13/2+ in the residual nuclei (after neutron evaporation) were observed, highlighting cluster-transfer as an interesting tool to populate such states in exotic nuclei.

6.4 Summary

In this work we studied the cluster-transfer reactions of the ^{98}Rb + ^{7}Li system in order to gain experience with both the experimental and theoretical aspects of the reactions, focusing on the α- and triton-transfer channels.

The analysis work for this master thesis focused on the detected particles. The elastic scattering was analyzed in detail to determine a normalization for the differential cross-sections of the transfer channels and to extract the average beam intensity.

The preparatory goal of this work has been achieved yielding some very useful insights. Most importantly, we have observed the cross-sections for α- and triton transfer to be larger than expected, approximately 20 mb and 5 mb in range of 22°- 41° (lab), which make the reaction feasible for studies with low intensity RIBs. Secondly, we observed the population of high spin states in the residual nuclei after neutron evaporation, up to 13/2+.

Transfer to a very high excitation energy in the residual nucleus was observed, and interpreted as a common characteristic of cluster-transfer. This high excitation energy leads to the evaporation of several neutrons, which inhibits the production of nuclei more neutron rich than the beam.

The high excitation energy also has consequences for the detection of the α-particles and tritons. Their identification at angles greater the approximately 60° (lab) is not possible with the ΔE-E technique due to the decreased kinetic energy.

Preliminary theoretical calculations in a CDCC approach described rather well the α- and triton-transfer channels as a direct process. The experimentally observed ratio between these two channels was well reproduced by the theory, and the calculated absolute cross-sections were within the observed order of magnitude. This indicates that the description of cluster-transfer from ^{7}Li as the transfer of a cluster to continuum states in the residual nucleus is valid in this particular case.

As a tool to probe exotic nuclei at high angular momenta, cluster-transfer reactions are feasible. Their limitations and challenges were made obvious in this work, and should be considered in depth when proposing this reaction mechanism as a means to populate specific nuclei.

Bibliography

[1] B A Brown and B H Wildenthal. Status of the nuclear shell model. *Annual Review of Nuclear and Particle Science*, 38(1):29–66, 1988. doi: 10.1146/annurev.ns.38.120188.000333. URL http://www.annualreviews.org/doi/abs/10.1146/annurev.ns.38.120188.000333.

[2] Maria Goeppert Mayer. Nuclear configurations in the spin-orbit coupling model. i. empirical evidence. *Phys. Rev.*, 78:16–21, Apr 1950. doi: 10.1103/PhysRev.78.16. URL http://link.aps.org/doi/10.1103/PhysRev.78.16.

[3] Sven G osta Nilsson. Binding states of individual nucleons in strongly deformed nuclei. *Dan. Mat. Fys. Medd.*, 29(CERN-55-30. 16):1–69. 69 p, 1955.

[4] B. Alex Brown. Islands of insight in the nuclear chart. *Physics*, 3:104, Dec 2010. doi: 10.1103/Physics.3.104. URL http://link.aps.org/doi/10.1103/Physics.3.104.

[5] Kris Heyde and John L. Wood. Shape coexistence in atomic nuclei. *Rev. Mod. Phys.*, 83:1467–1521, Nov 2011. doi: 10.1103/RevModPhys.83.1467. URL http://link.aps.org/doi/10.1103/RevModPhys.83.1467.

[6] Erich Kugler. The isolde facility. *Hyperfine Interactions*, 129(1-4):23–42, 2000. ISSN 0304-3843. doi: 10.1023/A:1012603025802.

[7] Y Blumenfeld, T Nilsson, and P Van Duppen. Facilities and methods for radioactive ion beam production. *Physica Scripta*, 2013(T152):14–23, 2013. URL http://stacks.iop.org/1402-4896/2013/i=T152/a=014023.

[8] K. Siwek-Wilczyńska, E. H. du Marchie van Voorthuysen, J. van Popta, R. H. Siemssen, and J. Wilczyński. Incomplete fusion in ^{12}C + ^{160}Gd collisions interpreted in terms of a generalized concept of critical angular momentum. *Phys. Rev. Lett.*, 42:1599–1602, Jun 1979. doi: 10.1103/PhysRevLett.42.1599. URL http://link.aps.org/doi/10.1103/PhysRevLett.42.1599.

[9] R. M. Clark et al. Population of nuclei via ^{7}Li-induced binary reactions. *Phys. Rev. C*, 72:054605, Nov 2005. doi: 10.1103/PhysRevC.72.054605. URL http://link.aps.org/doi/10.1103/PhysRevC.72.054605.

[10] G. D. Dracoulis et al. Incomplete fusion as a specroscopic tool. *J. Phys. G: Nucl. Part. Phys.*, 23:1191, 1997.

[11] ISOLDE. Gamma spectroscopy of n-rich ^{95,96}Rb nuclei by the incomplete fusion reaction of ^{94}Kr on ^{7}Li: Introduction to HIE-ISOLDE studies of n-rich Sb and Tl isotopes with sn and hg radioactive beams, Feb 2012.

[12] P Van Duppen and K Riisager. Physics with rex-isolde: from experiment to facility. *Journal of Physics G: Nuclear and Particle Physics*, 38(2):024005, 2011. URL http://stacks.iop.org/0954-3899/38/i=2/a=024005.

[13] J. P. Bondorf, F. Dickmann, D. H. E. Gross, and P. J. Siemens. Statistical aspects of heavy-ion reactions. *J. Phys. Colloques*, 32(C6):C6–145–C6–149, 1971. doi: 10.1051/jphyscol:1971623. URL http://dx.doi.org/10.1051/jphyscol:1971623.

[14] J. Wilczyński, K. Siwek-Wilcyńska, et al. Incomplete-fusion reactions in the ^{14}N+^{159} Tb system and a "sum-rule model" for fusion and incomplete-fusion reactions. *Phys. Rev. Let.*, 45(8):606–609, 1980.

[15] J. Wilczynski. Calculations of the critical angular momentum in the entrance reaction channel. *Nuclear Physics A*, 216(2):386 – 394, 1973. ISSN 0375-9474. doi: 10.1016/0375-9474(73)90474-0. URL http://www.sciencedirect.com/science/article/pii/0375947473904740.

[16] J. Wilczynski, K. Siwek-Wilczynska, J. Van Driel, S. Gonggrijp, D.C.J.M. Hageman, R.V.F. Janssens, J. Lukasiak, R.H. Siemssen, and S.Y. Van Der Werf. Binary l-matched reactions in 14n + 159tb collisions. *Nuclear Physics A*, 373(1):109 – 140, 1982. ISSN 0375-9474. doi: http://dx.doi.org/10.1016/0375-9474(82)90183-X. URL http://www.sciencedirect.com/science/article/pii/037594748290183X.

[17] J Nyberg, A Johnson, S A Hjorth, A Kerek, C G Lindén, S E Arnell, S Mattsson, H A Roth, and O Skeppstedt. Angular momentum transfer in reactions induced by 14 n ions on 154 sm. *Physica Scripta*, 33(3):206, 1986. URL http://stacks.iop.org/1402-4896/33/i=3/a=004.

[18] K. Siwek-Wilczynska, E.H.du Marchie van Voorthuysen, J. van Popta, R.H. Siemssen, and J. Wilczynski. Incomplete fusion in 12c+160gd collisions. *Nuclear Physics A*, 330(1):150 – 172, 1979. ISSN 0375-9474. doi: http://dx.doi.org/10.1016/0375-9474(79)90542-6. URL http://www.sciencedirect.com/science/article/pii/0375947479905426.

[19] Bhushan Bhujang, Pragya Das, R P Singh, R Tripathi, and B S Tomar. Incomplete fusion studies near coulomb barrier: a modified sum rule model. *Journal of Physics: Conference Series*, 420(1):012128, 2013. URL http://stacks.iop.org/1742-6596/420/i=1/a=012128.

[20] G.R̃. Satchler. *Introduction to nuclear reactions*. Macmillan, 2 edition, 1990.

[21] XIE Wenfang and CHEN Chuanyu. A generalized talmi-moshinsky trans. *Communications in Theoretical Physics*, page 419, 1998.

[22] Ian Thompson and Filomena Nunes. *Nuclear reactions for astrophysics*. Cambridge University Press, 2009.

[23] I. J. Thompson. Coupled reaction channels calculations in nuclear physics. *Comput. Phys. Rep.*, 7:167, 1988.

[24] Vinzenz Bildstein et al. T-rex. *The European Physical Journal A - Hadrons and Nuclei*, 48:1–10, 2012. ISSN 1434-6001. URL http://dx.doi.org/10.1140/epja/i2012-12085-6. 10.1140/epja/i2012-12085-6.

[25] N. Warr, J. Walle, et al. The miniball spectrometer. *The European Physical Journal A*, 49(3):1–32, 2013. ISSN 1434-6001. doi: 10.1140/epja/i2013-13040-9. URL http://dx.doi.org/10.1140/epja/i2013-13040-9.

[26] Target and MINIBALL. http://isolde.web.cern.ch/ISOLDE/REX-ISOLDE/miniball.html, 2010.

[27] Micron Semiconductor Ltd., 2013. URL http://www.micronsemiconductor.co.uk. accessed 30 July 2013.

[28] S. Klupp. Documentation of the calibration of the T-REX detectors and of MINIBALL, October 2012.

[29] R. Bass. *Nuclear Reactions with Heavy Ions*. Texts and monographs in physics. Springer, 1980. ISBN 9783540096115. URL http://books.google.be/books?id=tgx2QgAACAAJ.

[30] D.M. Brink. Kinematical effects in heavy-ion reactions. *Physics Letters B*, 40(1):37 – 40, 1972. ISSN 0370-2693. doi: http://dx.doi.org/10.1016/0370-2693(72)90274-2. URL http://www.sciencedirect.com/science/article/pii/0370269372902742.

[31] S. Agostinelli et al. Geant4—a simulation toolkit. *Nuc. Inst. and Meth. Phys. A*, 506(3):250 – 303, 2003. ISSN 0168-9002. doi: http://dx.doi.org/10.1016/S0168-9002(03)01368-8. URL http://www.sciencedirect.com/science/article/pii/S0168900203013688.

[32] O.B̃. Tarasov and D. Bazin. Lise++: Radioactive beam production with in-flight separators. *Nuc. Inst. and Meth. Phys. B*, 266(19–20):4657 – 4664, 2008. ISSN 0168-583X. doi: http://dx.doi.org/10.1016/j.nimb.2008.05.110. URL http://www.sciencedirect.com/science/article/pii/S0168583X08007969.

[33] JamesF. Ziegler and JochenP. Biersack. The stopping and range of ions in matter. In D.Allan Bromley, editor, *Treatise on Heavy-Ion Science*, pages 93–129. Springer US, 1985. ISBN 978-1-4615-8105-5. doi: 10.1007/978-1-4615-8103-1_3. URL http://dx.doi.org/10.1007/978-1-4615-8103-1_3.

[34] A Werbrouck. Kinematics and multiparticle systems, 1968.

[35] J. Cook. Global optical-model potentials for the elastic scattering of ^{6,7}Li projectiles. *Nuc. Phys. A*, 388(1):153 – 172, 1982. ISSN 0375-9474. doi: http://dx.doi.org/10.1016/0375-9474(82)90513-9.

[36] Fimiani, L., Figueira, J.M., Martí, G.V., Testoni, J.E., Arazi, A., Capurro, O.A., Cárdenas, W.H.Z., Cardona, M.A., Carnelli, P., de Barbará, E., Hojman, D., Martinez Heimann, D., Negri, A.E., and Pacheco, A.J. Ince of projectile breakup in the elastic scattering of the systems 6,7li+80se. *EPJ Web of Conferences*, 17:03003, 2011.

doi: 10.1051/epjconf/20111703003. URL http://dx.doi.org/10.1051/epjconf/20111703003.

[37] A. Shrivastava, A. Navin, A. Diaz-Torres, V. Nanal, K. Ramachandran, M. Rejmund, S. Bhattacharyya, A. Chatterjee, S. Kailas, A. Lemasson, R. Palit, V.V. Parkar, R.G. Pillay, P.C. Rout, and Y. Sawant. Role of the cluster structure of 7li in the dynamics of fragment capture. *Physics Letters B*, 718(3):931 – 936, 2013. ISSN 0370-2693. doi: http://dx.doi.org/10.1016/j.physletb.2012.11.064. URL http://www.sciencedirect.com/science/article/pii/S0370269312012300.

[38] A. Diaz-Torres, D. J. Hinde, J. A. Tostevin, M. Dasgupta, and L. R. Gasques. Relating breakup and incomplete fusion of weakly bound nuclei through a classical trajectory model with stochastic breakup. *Phys. Rev. Lett.*, 98:152701, Apr 2007. doi: 10.1103/PhysRevLett.98.152701. URL http://link.aps.org/doi/10.1103/PhysRevLett.98.152701.

Instituut voor Kern- en Stralingsfysica
Celestijnenlaan 200D
3001 HEVERLEE, BELGIË
tel. + 32 16 32 72 63
fax + 32 16 32 79 85
fys.kuleuven.be/iks